

Air Force Institute of Technology

**AFIT Scholar**

---

Theses and Dissertations

Student Graduate Works

---

6-2022

## Effects of Motion Measurement Errors on Radar Target Detection

Darnell D. Parker

Follow this and additional works at: <https://scholar.afit.edu/etd>



Part of the [Signal Processing Commons](#)

---

### Recommended Citation

Parker, Darnell D., "Effects of Motion Measurement Errors on Radar Target Detection" (2022). *Theses and Dissertations*. 5482.

<https://scholar.afit.edu/etd/5482>

This Thesis is brought to you for free and open access by the Student Graduate Works at AFIT Scholar. It has been accepted for inclusion in Theses and Dissertations by an authorized administrator of AFIT Scholar. For more information, please contact [richard.mansfield@afit.edu](mailto:richard.mansfield@afit.edu).



**EFFECTS OF MOTION MEASUREMENT  
ERRORS ON RADAR TARGET DETECTION**

THESIS

Darnell D Parker, Capt, USAF

AFIT-ENG-MS-22-J-015

**DEPARTMENT OF THE AIR FORCE  
AIR UNIVERSITY**

***AIR FORCE INSTITUTE OF TECHNOLOGY***

**Wright-Patterson Air Force Base, Ohio**

DISTRIBUTION STATEMENT A  
APPROVED FOR PUBLIC RELEASE; DISTRIBUTION UNLIMITED.

The views expressed in this document are those of the author and do not reflect the official policy or position of the United States Air Force, the United States Department of Defense or the United States Government. This material is declared a work of the U.S. Government and is not subject to copyright protection in the United States.

AFIT-ENG-MS-22-J-015

EFFECTS OF MOTION MEASUREMENT ERRORS ON RADAR TARGET  
DETECTION

THESIS

Presented to the Faculty  
Department of Electrical and Computer Engineering  
Graduate School of Engineering and Management  
Air Force Institute of Technology  
Air University  
Air Education and Training Command  
in Partial Fulfillment of the Requirements for the  
Degree of Master of Science in Electrical Engineering

Darnell D Parker, B.S.E.E.

Capt, USAF

June 16, 2022

DISTRIBUTION STATEMENT A  
APPROVED FOR PUBLIC RELEASE; DISTRIBUTION UNLIMITED.

AFIT-ENG-MS-22-J-015

EFFECTS OF MOTION MEASUREMENT ERRORS ON RADAR TARGET  
DETECTION

THESIS

Darnell D Parker, B.S.E.E.  
Capt, USAF

Committee Membership:

Julie A Jackson, Ph.D  
Chair

Lt Col James R Lievsay, Ph.D  
Member

Lt Col Michael D Seal, Ph.D  
Member

## Acknowledgements

First and foremost, thanks go to God for getting me to where I am today. Next, a big thank you go to my loving wife and children for enduring the long hours, days, and months that I spent working on this thesis, rather than spending time with them. Finally, thanks go to Dr. Julie Jackson for her kind words, advice, and support throughout this entire journey, and to Lt Col Lievsay and Lt Col Seal for their comments and suggestions on my thesis. I could not have done it without you!

Darnell D Parker

## Abstract

Synthetic aperture radars are popular for both military and commercial purposes due to their ability to penetrate cloud cover and produce images in low-light/nighttime conditions. However, the process necessary to produce such images is complex, with many potential paths leading to image distortion and ultimately task failure. At any point during the radar's imaging process, from the initial signal transmission to the collection of raw data to its transformation into intelligible image products, events could occur that have varying effects on the utility of the final product. Occurrences such as high clutter returns and the presence of motion measurement errors, leading to low image quality, are of primary concern. Understanding how decreases in image quality affect task performance would assist radar engineers in focusing their attentions towards data collection issues that would provide the greatest reward through resolution. This thesis explores the relationships present between signal-to-clutter ratios, motion measurement errors, image quality metrics, and the task of target detection, in order to identify which factor to focus on in order to attain the highest probability of detection success. This investigation is accomplished by executing a high number of Monte Carlo trials through a coherent target detector and analyzing the results. The aforementioned relationships are demonstrated via sample synthetic aperture radar imagery, histograms, receiver operating characteristic curves, and error bar plots.

# Table of Contents

	Page
Acknowledgements . . . . .	iv
Abstract . . . . .	v
List of Figures . . . . .	viii
List of Tables . . . . .	x
I. Introduction . . . . .	1
1.1 Problem Background . . . . .	1
1.2 Research Goals and Contributions . . . . .	1
1.3 Assumptions . . . . .	2
1.4 Thesis Overview . . . . .	3
II. Background and Literature Review . . . . .	4
2.1 Synthetic Aperture Radar . . . . .	4
2.1.1 SAR Geometry . . . . .	4
2.1.2 Spatial Frequency Domain . . . . .	6
2.1.3 Scene Reflectivity and Ideal Phase History . . . . .	9
2.1.4 SAR Image Formation . . . . .	13
2.1.5 Point Spread Function . . . . .	14
2.1.6 Motion Measurement Errors . . . . .	18
2.2 Image Quality Metrics . . . . .	23
2.2.1 Contrast . . . . .	24
2.2.2 Sharpness . . . . .	25
2.2.3 Entropy . . . . .	25
III. SAR Imaging Process and CFAR Detector Setup . . . . .	27
3.1 Overview . . . . .	27
3.2 Complete Phase History Model . . . . .	27
3.3 SAR Image Grid . . . . .	29
3.4 Statistics of a Pixel . . . . .	30
3.5 Target Detection . . . . .	33
3.6 Number of Required Monte Carlo Trials . . . . .	42
IV. Results and Analysis . . . . .	44
4.1 Overview . . . . .	44
4.2 Simulation Setup . . . . .	44
4.3 Effects of Motion Measurement Errors . . . . .	48



	Page
4.4 Target Detection Performance .....	55
4.5 IQM Analysis .....	60
4.5.1 Contrast .....	61
4.5.2 Sharpness .....	65
4.5.3 Entropy .....	67
V. Conclusions .....	71
5.1 Key Conclusions .....	71
5.2 Significance of the Research .....	72
5.3 Future Work .....	72
Bibliography .....	74
Acronyms .....	78

## List of Figures

Figure		Page
1	The SAR geometry utilized in this thesis . . . . .	5
2	Spatial Domain . . . . .	8
3	Spatial Frequency Domain . . . . .	9
4	PSF Images with Differing Range and Cross-Range Values . . . . .	17
5	Effects of Various Along-Track Velocity Errors on SAR Image with Point Scatterer at (0,0) . . . . .	21
6	Effects of Various Along-Track Acceleration Errors . . . . .	22
7	Plot of all simulated point scatterers; blue points represent clutter, and red point represents a target point scatterer stacked on top of a clutter point scatterer . . . . .	39
8	Depiction of CFAR stencil used for target detection in this simulation. . . . .	40
9	Image and Probability Distributions of Target and Clutter Pixel Magnitudes for Images using Different SCRs . . . . .	47
10	Probability Densities of Target and Clutter Pixel Magnitudes in Images with SCR of 25, after applying varying levels of position measurement error . . . . .	50
11	Histograms of Target and Clutter Pixel Magnitudes in Images of SCR = 25, after applying varying levels of velocity measurement error . . . . .	51
12	Histograms of Target and Clutter Pixel Magnitudes in Images of SCR = 25, after applying varying levels of acceleration measurement error . . . . .	53
13	Histograms of Target and Clutter Pixel Magnitudes in Images of SCR = 1, after applying varying levels of motion measurement errors . . . . .	54
14	ROC Curves with varying levels of motion measurement errors applied, for each SCR . . . . .	57

Figure		Page
15	Highest Simulated Probability of Detection for each MME applied, at each SCR .....	58
16	Contrast 1 Metrics for each MME at each SCR .....	62
17	Contrast 2 Metrics for each MME at each SCR .....	64
18	Sharpness Metrics for each MME at each SCR .....	66
19	Entropy 1 Metrics for each MME at each SCR .....	68
20	Entropy 2 Metrics for each MME at each SCR .....	70

## List of Tables

Table		Page
1	Minimum number of realizations needed for different standards of deviation at 95% confidence in $\pm 0.1$ amplitude error . . . . .	43
2	SAR Simulation Parameters . . . . .	44
3	Theoretical vs Simulated Target Reflectivity Amplitude Statistics . . . . .	45
4	Theoretical vs Simulated Target Pixel Statistics . . . . .	46
5	Theoretical vs Simulated Clutter Pixel Statistics . . . . .	46
6	Theoretical vs Simulated Clutter Pixel Statistics . . . . .	48
7	Highest PDs Achieved for each SCR/MME Combination . . . . .	56
8	Normalized Mean Contrast 1 Values at each MME and SCR level . . . . .	61
9	Normalized Mean Contrast 2 Values at each MME and SCR level . . . . .	63
10	Normalized Mean Sharpness Values at each MME and SCR level . . . . .	65
11	Normalized Mean Entropy 1 Values at each MME and SCR level . . . . .	67
12	Normalized Mean Entropy 2 Values at each MME and SCR level . . . . .	69

# EFFECTS OF MOTION MEASUREMENT ERRORS ON RADAR TARGET DETECTION

## I. Introduction

### 1.1 Problem Background

There are a wide variety of radar operations, ranging from military applications such as search/track, air defense, and instrumentation, to commercial uses such as weather tracking, terrain mapping, and ground penetration [1,2]. Intelligible radar image products are integral to the completion of these tasks, so data quality control is of utmost importance. There are many commonly used data quality metrics that are useful in assessing radar data quality [3–5]; however, meeting a specific data quality metric does not always indicate that the data product possesses the right type of quality needed for a particular task, such as target detection. This thesis examines the application of different image quality metrics to SAR images and their relationships with the probability of target detection.

### 1.2 Research Goals and Contributions

The goal of this research is to study various radar image quality metrics (IQMs) and assess their individual connections with target detection performance metrics. This research will be accomplished by first simulating the radar data processing chain to produce large sets of images utilizing different signal-to-clutter ratios (SCRs). Varying amounts of motion measurement error (MME) will then be injected into the image formation process to produce images of degraded quality; Monte Carlo target

detection trials will be run on the degraded images, resulting in quantitative representations of how much image degradation affects target detection. Selected IQMs will also be computed to assess the degree of quality degradation, permitting data trend examination and determination of relationships between the image quality metrics and target detection success. This thesis will link IQMs with motion measurement errors and target detection success, and discuss which IQMs should be considered as the best indicators for target detection success.

### 1.3 Assumptions

Some key assumptions were made for research purposes. They are as follows:

- The SAR signal encounters the same amount of propagation effects as it travels through the surrounding environment, each and every time the signal is transmitted. This facilitates accurate assessment of the results of the Monte Carlo trials, without concern over the varied effects of this additional factor.
- The SAR system employed in this thesis inhibits system noise to a level that is negligible in comparison to target and clutter returns, directing focus on signal-to-clutter ratios as opposed to signal-to-clutter-plus-noise ratios.
- There is a complete absence of interference from other sources of RF energy.
- All point scatterers within the target scene are stationary through the duration of signal transmission and reflection back to the receiver.
- SAR spotlight mode operation is utilized, as opposed to SAR stripmap mode.
- Phase history is acquired through straight and level broadside acquisition.
- A monostatic radar configuration is employed, as opposed to a bistatic or multistatic configuration.
- The target scene is on flat ground (i.e., there are no changes in target elevation).
- The ground range and slant range are large enough to be considered as constants

with respect to slow time.

- The radar platform follows a level flight path with constant velocity.

## **1.4 Thesis Overview**

The rest of the thesis is organized as follows: Chapter II provides fundamental knowledge regarding the SAR system environment, the radar imaging process, and metrics that will be used to judge image quality. Chapter III explains the phase history models and detector algorithms utilized in researching this thesis. Chapter IV details the setup of the simulations, presents the results, and discusses observations of the results. Finally, all key findings are summarized in Chapter V, followed by recommendations for future works.

## II. Background and Literature Review

This chapter provides the necessary framework to understand the simulation setup and results discussed in the following chapters. To this end, an overview of the radar data collection and processing chain, and a description of basic SAR imaging concepts, are presented.

### 2.1 Synthetic Aperture Radar

SAR is a coherent imaging radar based on the concept of synthesizing a very long antenna, primarily by transmitting a signal from a small antenna moving along a platform flight path and then processing the signal's reflection [6]. Both amplitude and phase of the received signal must be recorded in order to synthesize the receiving antenna. The principal product of a SAR system is a two-dimensional image depicting the reflective intensity of scatterers positioned in the illuminated area. Higher range resolution is achieved by increasing signal bandwidth and implementing pulse compression techniques [7]; meanwhile, azimuth (cross-range) resolution is related to the synthetic aperture length and the antenna's distance from target scene, along with associated matched filters and data transformations.

There are a few basic concepts to understand when discussing how SAR signal data is transformed into intelligible images, including SAR geometry, scene reflectivity, phase history, and MMEs. These topics will be further explained and discussed below.

#### 2.1.1 SAR Geometry

The radar data collection process involves transmitting RF energy towards a particular scene of interest, where it is reflected off of scatterers within the target scene;



a portion of the transmitted energy then propagates back the SAR receiver. This thesis assumes a monostatic SAR system, meaning that the signal's transmitter and receiver are co-located on the same platform, as opposed to bistatic or multistatic systems where the transmitter(s) are located on a platform separate from the receiver(s). Figure 1 depicts the axes, angles, and paths that must be considered when discussing a SAR system; they are defined as follows:

- The azimuth angle subtended by the SAR platform during signal transmission and reception, with respect to scene center, is represented by  $\phi$ , while  $\Delta\phi$  describes the distance traveled by the SAR platform while fulfilling the azimuth angle. This distance is also referred to as *azimuth extent*, or *aperture length*.
- The grazing angle at which the SAR platform travels with respect to the target scene's ground plane is represented as  $\psi$ .
- The direction of the y-axis is parallel to the platform's flight path when  $\phi = 0$ ; this path can also be referred to as the *along-track* or *cross-range direction*. The

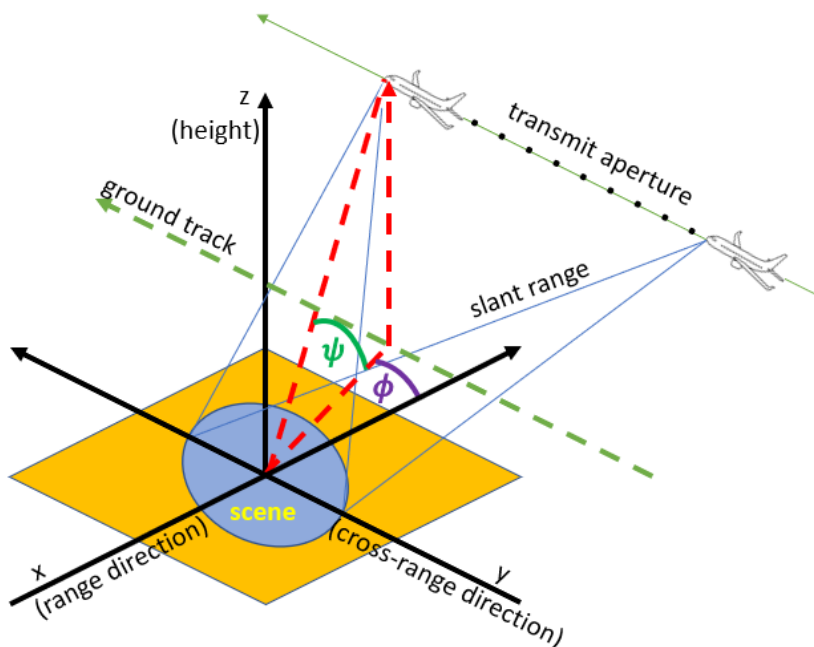


Figure 1: The SAR geometry utilized in this thesis

y-axis runs through the center of the target scene.

- The x-axis lies perpendicular to the y-axis along the ground plane, and runs through the center of both the target scene and the azimuth extent; this path is also referred to as the *range direction*. The intersection of the x- and y- axes is always presented as coordinates (0,0) in this thesis.
- The z-axis is perpendicular to both the x- and y-axis, and is used to denote the SAR platform's height.
- The particular SAR geometry utilized in this thesis is based on a right-handed coordinate system.

### 2.1.2 Spatial Frequency Domain

The SAR system relies on information gained from the *spatial frequency* domain in order to function. The spatial frequency domain is based on spatial frequency  $U$ , which follows the equivalency [7]

$$U = \frac{2\omega}{c} = \frac{4\pi f}{c} \quad (1)$$

where  $f$  represents all frequencies utilized to produce the radar signal, angular frequency is related to frequency as  $\omega = 2\pi f$ , and  $c$  represents the speed of light. SAR systems generally utilize a LFM “chirp” waveform to produce the signal used in illuminating the target scene; with this waveform, the signal frequency is altered in a linear fashion throughout frequency range  $\Delta f$  (or bandwidth  $B$ ) during pulse duration  $T$  for a chirp rate of  $\alpha$  rad/sec<sup>2</sup> or  $\gamma$  Hz<sup>2</sup>, such that  $\alpha = 2\pi\gamma = \frac{2\pi\Delta f}{T}$ . Signals produced using the LFM waveform can be modeled by [7–9]

$$s(t) = \text{rect}\left(\frac{t}{T}\right) \text{Re}\{e^{j(\omega_c t + \frac{\alpha t^2}{2})}\} = \text{rect}\left(\frac{t}{T}\right) \cos(2\pi f_c t + \pi\gamma t^2) \quad (2)$$

where  $\omega_c$  is the center frequency in radians,  $f_c$  is center frequency in Hertz, and

$$\text{rect}(t) = \begin{cases} 1 & \text{if } |t| \leq 0.5 \\ 0 & \text{if } |t| > 0.5 \end{cases}. \quad (3)$$

The instantaneous frequencies  $\omega_{inst}$  and  $f_{inst}$  are found by taking the time derivative of the phase, such that

$$\omega_{inst} = \frac{d}{dt}(2\pi f_c t + \pi \gamma t^2) = 2\pi(f_c + \gamma t) \quad (4)$$

$$f_{inst} = \frac{\omega_{inst}}{2\pi} = f_c + \gamma t. \quad (5)$$

Because  $t \in (-\frac{T}{2}, \frac{T}{2})$  and  $\gamma = \frac{\Delta f}{T} = \frac{B}{T}$ , equations (4) and (5) can be manipulated to see that the frequency is bounded as follows:

$$2\pi \left( f_c + \frac{\Delta f}{T} \left( -\frac{T}{2} \right) \right) \leq \omega_{inst} \leq 2\pi \left( f_c + \frac{\Delta f}{T} \left( \frac{T}{2} \right) \right) \quad (6)$$

$$f_c - \frac{B}{2} \leq f_{inst} \leq f_c + \frac{B}{2} \quad (7)$$

which simply shows that the instantaneous frequency is indeed bounded by its bandwidth ( $\Delta f = B$ ). For spatial frequency, substituting  $f_{inst}$  into (1) gives

$$\frac{4\pi f_c}{c} - \frac{2\pi \Delta f}{c} \leq U \leq \frac{4\pi f_c}{c} + \frac{2\pi \Delta f}{c} \quad (8)$$

$$U_c - \frac{2\pi B}{c} \leq U \leq U_c + \frac{2\pi B}{c} \quad (9)$$

and hence a spatial frequency range of

$$\Delta U = \frac{4\pi B}{c}. \quad (10)$$

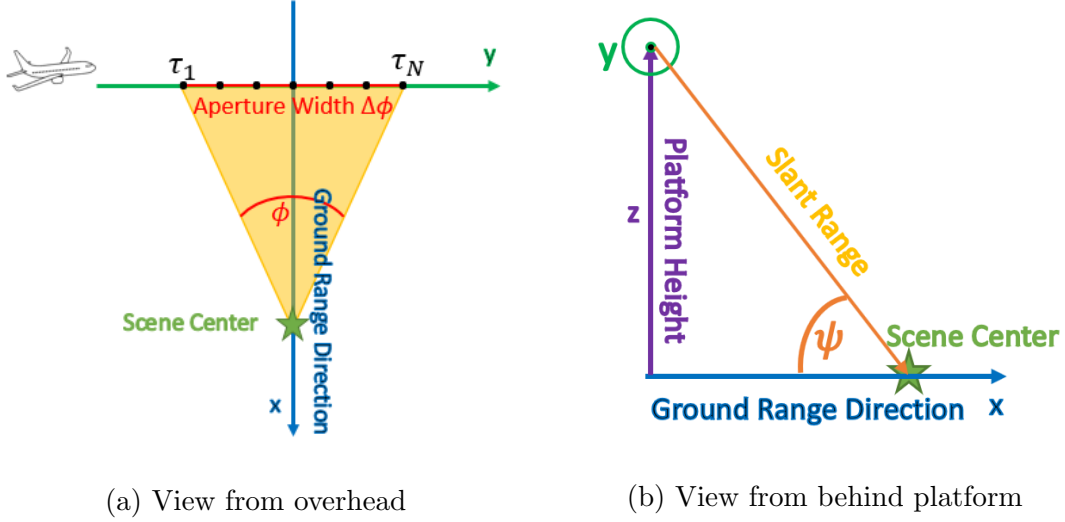


Figure 2: Spatial Domain

The projection-slice theorem states that the orientation of projections in the spatial domain can be used to specify “slices” in the spatial frequency domain [10]. Using the spatial geometry depicted in Figure 2a and 2b, spatial frequencies  $X$ ,  $Y$ , and  $Z$  are defined as

$$X = U \cos \phi = \frac{4\pi f \cos \phi}{c} \quad (11)$$

$$Y = U \sin \phi = \frac{4\pi f \sin \phi}{c} \quad (12)$$

$$Z = U \sin \psi = \frac{4\pi f \sin \psi}{c} \quad (13)$$

with  $X$  and  $Y$  lying in the slant range plane. Likewise, the spatial frequency bandwidths in the  $x$ - and  $y$ -directions on the slant range plane can be approximated as

$$\Delta X = \frac{4\pi \Delta f \cos \phi_c}{c} = \frac{4\pi \Delta f}{c} \quad (14)$$

$$\Delta Y = \frac{4\pi}{c} \left( 2f_c \sin \frac{\Delta \phi}{2} \right) = \frac{8\pi f_c \sin \frac{\Delta \phi}{2}}{c} \quad (15)$$

where  $\phi_c = 0^\circ$ , as shown in Figure 3. When considering spatial frequency as projected

into the ground range dimension, the expression needs to be multiplied by  $\cos \psi$ ; the spatial frequencies  $X$  and  $Y$  then become

$$X = \frac{4\pi f \cos \phi \cos \psi}{c} \quad (16)$$

$$Y = \frac{4\pi f \sin \phi \cos \psi}{c} \quad (17)$$

and the spatial frequency bandwidths become

$$\Delta X = \frac{4\pi \Delta f \cos \psi}{c} \quad (18)$$

$$\Delta Y = \frac{8\pi f_c \sin \frac{\Delta \phi}{2} \cos \psi}{c}. \quad (19)$$

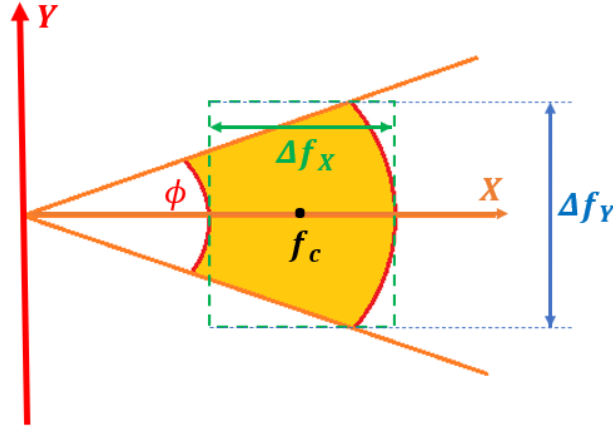


Figure 3: Spatial Frequency Domain

### 2.1.3 Scene Reflectivity and Ideal Phase History

In the previous section, the LFM chirp was briefly discussed. As this RF signal arrives at a reflective object, the signal energy induces an electric charge on the surface of the object that reradiates the incident signal. This reradiation is referred to as reflection or scattering; the amount of energy that is reflected (scattered) is

dependent on the size, shape, and composition of the illuminated target surface [1]. A SAR system's most basic function is to measure the (real or complex) reflectivity of a target surface; hence, a SAR image is ideally a representation of that reflectivity. The magnitude of an object's reflectivity can be represented by its radar cross section (RCS), whose formal definition [11] is

$$\sigma_{RCS} = \lim_{R \rightarrow \infty} 4\pi R^2 \frac{|\mathbf{E}_s|^2}{|\mathbf{E}_i|^2} \quad (20)$$

where  $R$  is the distance from the radar to the target scattering center,  $\mathbf{E}_i$  is the electric-field strength of the incident wave impinging on the target,  $\mathbf{E}_s$  is the electric-field strength of the scattered wave at the radar; note that both electric fields are vectors that depend on direction and signal frequency.

However, radar imaging does not directly measure RCS; rather, it attempts to estimate *target reflectivity*. Freeman provides a mathematical description of target reflectivity [12] as

$$g(x, y) = \sqrt{K_s} e^{j\phi_s} S_{pq}(x, y) \quad (21)$$

where  $S_{pq}(x, y)$  represents the complex amplitude data recorded by the SAR receiver as elements of the scattering matrix, and  $K_s$  and  $\phi_s$  are the gain and phase imposed on the data by the radar. Doring links the amplitude data with RCS [13] in the following formula:

$$S_{pq}(x, y) = \sqrt{\sigma_{RCS}} \delta(x, y) \quad (22)$$

where  $\delta(x, y)$  is the Dirac delta function. The combination of (21) and (22) leads to

$$g(x, y) = \sqrt{K_s \sigma_{RCS}} e^{j\phi_s} \delta(x, y) \quad (23)$$

In order to calculate the reflectivity for an entire object or scene, each scatterer

can be represented as a system of single-point isotropic nondispersive scatterers. This assumption creates what is called the *isotropic point model*, which can be written as [1]

$$g(x, y) = \sum_{m=1}^M A_m \delta(x - x_m, y - y_m). \quad (24)$$

In this thesis,  $A_m$  represents the complex amplitude of the  $m$ th isotropic point scatterer, where the amplitude density's variance retains equivalency to the  $\sqrt{K_s \sigma_{RCS}} e^{j\phi_s}$  term in (22).

After reflection off the target scene, the LFM signal propagates through the environment back to the radar receiver. The radar system then records the arrival times  $\tau_k$  of each LFM pulse, and the uniformly sampled frequencies  $f_i$  contained within each pulse; these two variables combine together to form what is known as *phase history* [7, 14]. The slow-time variable  $\tau_k$  can be replaced with  $\phi_k$ , the indexed angle at which the LFM pulse is transmitted and/or received (location of transmission and reception is the same under the move-stop-move assumption); the radar platform's position at  $\phi_k$  should coincide with its position at time  $\tau_k$ . The phase history of the total received SAR data, before deramp processing, can be modeled as the sum of the returns from all of the scatterers in the scene, such that [9]

$$G(U_i, \phi_k) = \sum_m A_m e^{j\Phi_m(f_i, \phi_k)} + \Omega \quad (25)$$

where  $A_m$  represents the same complex amplitude as described in (24),  $\Phi_m$  is the phase of the received SAR signal from the  $m$ th scatterer, and  $\Omega$  represents circular white Gaussian noise introduced by the receiver. For the purposes of this thesis, Gaussian noise is excluded from consideration, as it is generally dominated by the return from the scatterers. The phase history depicted in (25) is ideal because it does

not entail any type of errors at all; it is further defined by

$$\Phi_m(f_i, \phi_k) = -2\pi f_i \frac{\Delta R_m(\phi_k)}{c} = -\frac{U_i \Delta R_m(\phi_k)}{2} \quad (26)$$

where  $f_i$  is the  $i$ th sampled frequency from within the band  $f \in [f_c - \frac{B}{2}, f_c + \frac{B}{2}]$  and  $\tau_k$  is the time of the  $k$ th transmitted pulse as measured from the center of the radar aperture. The differential range  $\Delta R_m$  is the difference between the round-trip distance from the radar to scene center and the round-trip distance from the radar to the  $m$ th scatterer. Given platform ranges that are much larger than the size of the illuminated scene, a far-field assumption can be utilized to approximate the differential range [15] as

$$\Delta R_m(\phi_k) \approx -2x_m \cos \phi_k \cos \psi - 2y_m \sin \phi_k \cos \psi - 2z_m \sin \psi \quad (27)$$

where  $\phi_k$  is the azimuthal angle of the platform from scene center at time  $\tau_k$ , and  $\psi$  is the platform's grazing angle (which is equivalent to its elevation angle, due to flat earth and level flight path assumptions).

The ideal phase history can be used to derive a spatial frequency model of the scene reflectivity by substituting in the differential range equation and applying an



inverse Fourier transform [9], as follows:

$$G(U, \phi_k) = \sum_{m=1}^M A_m e^{jU \Delta R_m(\phi_k)/2} \quad (28)$$

$$= \sum_{m=1}^M A_m e^{jU(-2x_m \cos \phi_k \cos \psi - 2y_m \sin \phi_k \cos \psi - 2z_m \sin \psi)/2} \quad (29)$$

$$= \sum_{m=1}^M A_m e^{-j(x_m U \cos \phi_k \cos \psi + y_m U \sin \phi_k \cos \psi + z_m U \sin \psi)} \quad (30)$$

$$= \sum_{m=1}^M A_m e^{-j(x_m X_k + y_m Y_k + z_m Z_k)} \quad (31)$$

$$= \sum_{m=1}^M A_m \mathcal{F}[\delta(x - x_m, y - y_m, z - z_m)] \quad (32)$$

$$= \mathcal{F}\{g(x, y, z)\} \quad (33)$$

$$= G(X, Y, Z) \quad (34)$$

where  $G(U, \phi_k)$  is also known as the *range profile* at a specific aperture angle  $\phi_k$  achieved at slow-time pulse index  $k = 1, \dots, N_\tau$ .

#### 2.1.4 SAR Image Formation

Once phase history data has been collected, the data can then be converted into an intelligible image by employing one of several different methods, including matched filtering, backprojection, and polar reformatting [9]. Matched filtering is considered the mathematically ideal method of image formation process, while backprojection offers a slightly less rigorous and more efficient method. However, both of these methods require a vast number of computational operations, which may be too time-consuming for operational purposes. This thesis employs a PFA [7].

The need for PFA arises because, while the SAR system invariably collects samples of phase history using polar measurements, a FFT can only be applied to data

presented on a rectangular grid. Therefore, the polar phase history data needs to be reformatted into rectangular data in order to complete conversion into an image. PFA is accomplished using the following steps [7]:

1. Interpolate phase history data to a uniform grid in the range direction
2. Further interpolate the data to the same grid in the cross-range direction
3. Perform a two-dimensional IFFT on the reshaped data to form a SAR image

Note that it is important to set the number of frequency samples and slow-time pulses correctly to prevent aliasing in the range and cross-range dimensions, respectively. Such issues are normally avoided by setting image pixel size equal to the 2-D SAR resolution; this methodology will be utilized later in this thesis.

### 2.1.5 Point Spread Function

The PSF of a SAR image is equivalent to the impulse response of the SAR imaging system, or the output of processing the image of a single ideal point scatterer through that particular system. In Section 2.1.2, spatial frequency bandwidth was derived as

$$\Delta U = \frac{4\pi\Delta f}{c} \quad (35)$$

$$\Delta X = \frac{4\pi\Delta f \cos \psi}{c} \quad (36)$$

$$\Delta Y = \frac{8\pi f_c \sin \frac{\Delta\phi}{2} \cos \psi}{c} \quad (37)$$

The spatial frequency bandwidths in (36)-(37) provide a rectangular region of support for the phase history data; this region of support can be modeled as

$$H(X, Y) = \begin{cases} 1 & \text{if } |X - X_c| \leq \frac{\Delta X}{2} \text{ and } |Y - Y_c| \leq \frac{\Delta Y}{2} \\ 0, & \text{otherwise} \end{cases} \quad (38)$$

where  $X_c$  and  $Y_c$  are the center spatial frequencies in the x- and y-directions, respectively, and are modeled as

$$X_c = \frac{4\pi f_c \cos \psi}{c} \quad (39)$$

$$Y_c = \frac{8\pi f_c \sin \frac{\phi_c}{2} \cos \psi}{c} = 0. \quad (40)$$

Note that, because  $\phi_c = 0^\circ$  by definition,  $Y_c$  is also defined as zero as well. This region of support can also be represented as

$$H(X, Y) = \text{rect} \left( \frac{X - X_c}{\Delta X} \right) \text{rect} \left( \frac{Y - Y_c}{\Delta Y} \right) \quad (41)$$

$$= \delta(X - X_c, Y) * \text{rect} \left( \frac{X}{\Delta X} \right) \text{rect} \left( \frac{Y}{\Delta Y} \right) \quad (42)$$

where  $*$  denotes convolution. Now, by applying an inverse Fourier transform to the region of support  $H(X, Y)$ , the PSF for the SAR system is derived as

$$\begin{aligned} h(x, y) &= \Delta X \Delta Y e^{jX_c x} \text{sinc} \left( \frac{x \Delta X}{2\pi} \right) \text{sinc} \left( \frac{y \Delta Y}{2\pi} \right) \\ &= \frac{32\pi^2 f \Delta f \sin \frac{\Delta \phi}{2} \cos^2 \psi}{c^2} e^{jX_c x} \text{sinc} \left( \frac{2x \Delta f \cos \psi}{c} \right) \text{sinc} \left( \frac{4y f_c \sin \frac{\Delta \phi}{2} \cos \psi}{c} \right) \end{aligned} \quad (43)$$

where the sinc function is defined by [7]

$$\text{sinc}(a) = \begin{cases} \frac{\sin(\pi a)}{\pi a} & a \neq 0 \\ 1 & a = 0 \end{cases} \quad (44)$$

The term *resolution* refers to the minimum distance necessary between two point scatterers to allow them to be distinguishable in a SAR image. Range resolution can

be derived as

$$\rho_x = \frac{2\pi}{\Delta X} = \frac{c}{2\Delta f \cos \psi} = \frac{c}{2B \cos \psi} \quad (45)$$

in the ground plane (as opposed to the slant range plane), while ground cross-range resolution is derived as

$$\rho_y = \frac{2\pi}{\Delta Y} = \frac{c}{4f_c \sin \frac{\Delta \phi}{2} \cos \psi} = \frac{\lambda_c}{4 \sin \frac{\Delta \phi}{2} \cos \psi} \quad (46)$$

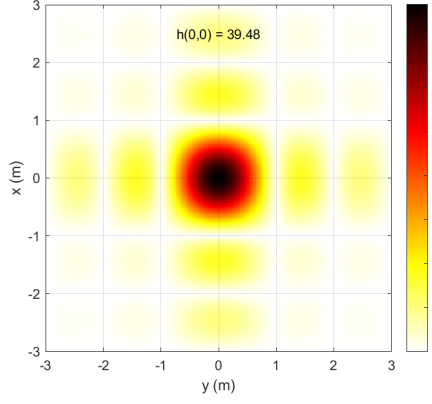
where  $\lambda_c$  is the center wavelength utilized by the SAR system during RF transmission. Substituting the resolution calculations (45) and (46) into (43) leaves a much simpler formula for PSF:

$$h(x, y) = \frac{4\pi^2 e^{jX_c x}}{\rho_x \rho_y} \text{sinc} \left( \frac{x}{\rho_x} \right) \text{sinc} \left( \frac{y}{\rho_y} \right) \quad (47)$$

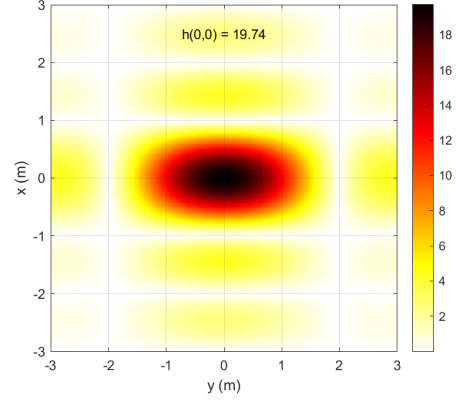
Figures 4a-4d display images of PSFs formed using PFA with different range and crossrange resolution combinations; note that the amplitude of the PSF at coordinates (0,0) match the expected output from inserting those coordinates into (47). For example, for both a range and crossrange resolution of 1 ( $\rho_x = \rho_y = 1$ ):

$$h(0, 0) = \frac{4\pi^2 e^{jX_c x}}{\rho_x \rho_y} \text{sinc} \left( \frac{x}{\rho_x} \right) \text{sinc} \left( \frac{y}{\rho_y} \right) \quad (48)$$

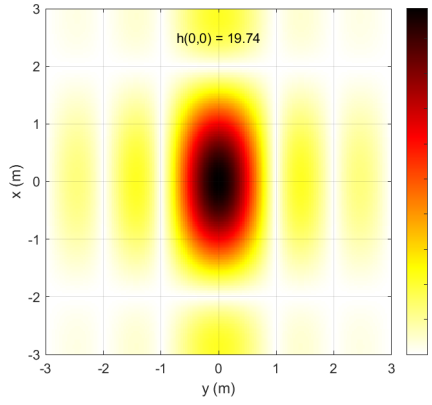
$$= \frac{4\pi^2 e^{jX_c(0)}}{(1)(1)} \text{sinc} \left( \frac{0}{1} \right) \text{sinc} \left( \frac{0}{1} \right) = 4\pi^2 = 39.478 \quad (49)$$



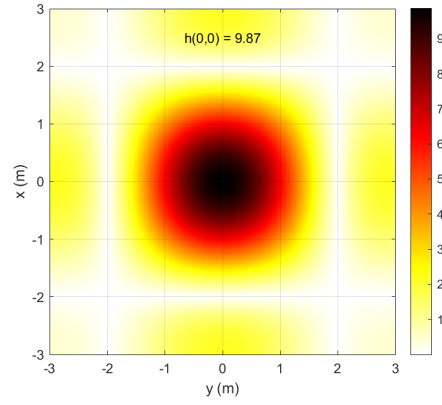
(a)  $\rho_x = 1$  m,  $\rho_y = 1$  m



(b)  $\rho_x = 2$  m,  $\rho_y = 1$  m



(c)  $\rho_x = 1$  m,  $\rho_y = 2$  m



(d)  $\rho_x = 2$  m,  $\rho_y = 2$  m

Figure 4: PSF Images with Differing Range and Cross-Range Values

### 2.1.6 Motion Measurement Errors

Equation (25) gives an ideal phase history achieved through the exact and precise measurement of platform motion that is devoid of even the slightest amount of deviation; unfortunately, such error-free measurements are impossible under real-world conditions. The presence of MMEs are unavoidable, and therefore must be reflected in the calculation of the phase history data, as

$$G_\epsilon = \sum_m A_m e^{j\hat{\Phi}_m}. \quad (50)$$

Equation (50) reflects the phase history data with phase errors

$$\hat{\Phi}_m = -\frac{2\pi f_i \Delta \hat{R}_m(\phi_k)}{c} = -\frac{U_i \Delta \hat{R}_m(\phi_k)}{2}, \quad (51)$$

where the differential range calculation now includes both the true differential range between scene center and the  $m$ th scatterer, as derived in (27), and the amount of differential range deviation caused by errors in motion measurement:

$$\Delta \hat{R}_m(\phi_k) = \Delta R_m(\phi_k) + \Delta \tilde{R}_r(\phi_k). \quad (52)$$

The differential range error can be expressed in a manner similar to that found in (27),

$$\Delta \tilde{R}_r(\phi_k) \approx -2\tilde{x}_r \cos \phi_k \cos \psi - 2\tilde{y}_r \sin \phi_k \cos \psi - 2\tilde{z}_r \sin \psi \quad (53)$$

where  $(\tilde{x}_r, \tilde{y}_r, \tilde{z}_r)$  are the total location measurement errors for the SAR platform, but in order to examine the effects of MMEs on SAR image formation, the errors must be explicitly linked to both the position and motion of the radar. This can be

done by first making the assumptions that the ground range  $r = \sqrt{x_r^2 + y_r^2}$  and slant range  $R = \sqrt{x_r^2 + y_r^2 + z_r^2}$ , with true radar position  $(x_r, y_r, z_r)$ , are large enough to be considered as constants with respect to slow time  $\tau$ , and that the platform is following a linear flight path with constant velocity [1, 7–9]. Following Rigling’s model in [9], these assumptions permit the linear approximations

$$\cos \phi_k \approx \frac{x_r + v_x \tau_k}{r} \quad (54a)$$

$$\sin \phi_k \approx \frac{y_r + v_y \tau_k}{r} \quad (54b)$$

$$\cos \psi \approx \frac{r}{R} \quad (54c)$$

$$\sin \psi \approx \frac{z_r + v_z \tau_k}{R} \quad (54d)$$

where  $(v_x, v_y, v_z)$  is the true velocity of the SAR platform in the x-, y-, and z-directions. By combining (53) with (54), the differential range can now be expressed as

$$\Delta R_m(\tau_k) \approx -2x_m \frac{x_r + v_x \tau_k}{R} - 2y_m \frac{y_r + v_y \tau_k}{R} - 2z_m \frac{z_r + v_z \tau_k}{R} \quad (55)$$

while the differential range error can be expressed as

$$\Delta \tilde{R}_r(\tau_k) \approx -2\tilde{x}_r \frac{x_r + v_x \tau_k}{R} - 2\tilde{y}_r \frac{y_r + v_y \tau_k}{R} - 2\tilde{z}_r \frac{z_r + v_z \tau_k}{R}. \quad (56)$$

Low-frequency MMEs are often modeled as [9]

$$\begin{bmatrix} \tilde{x}_r \\ \tilde{y}_r \\ \tilde{z}_r \end{bmatrix} = \begin{bmatrix} \tilde{p}_x \\ \tilde{p}_y \\ \tilde{p}_z \end{bmatrix} + \begin{bmatrix} \tilde{v}_x \\ \tilde{v}_y \\ \tilde{v}_z \end{bmatrix} \tau_k + \begin{bmatrix} \tilde{a}_x \\ \tilde{a}_y \\ \tilde{a}_z \end{bmatrix} \frac{\tau_k^2}{2} \quad (57)$$

where  $(\tilde{p}_x, \tilde{p}_y, \tilde{p}_z)$ ,  $(\tilde{v}_x, \tilde{v}_y, \tilde{v}_z)$ , and  $(\tilde{a}_x, \tilde{a}_y, \tilde{a}_z)$  represent errors in the measurement of the radar platform’s position, velocity, and acceleration, respectively. These motion

measurement errors, when combined with Equation (56), result in

$$\begin{aligned}\Delta\tilde{R}_r(\tau_k) \approx & -2 \left( \tilde{p}_x + \tilde{v}_x\tau_k + \tilde{a}_x\frac{\tau_k^2}{2} \right) \frac{x_r + v_x\tau_k}{R} \\ & -2 \left( \tilde{p}_y + \tilde{v}_y\tau_k + \tilde{a}_y\frac{\tau_k^2}{2} \right) \frac{y_r + v_y\tau_k}{R} \\ & -2 \left( \tilde{p}_z + \tilde{v}_z\tau_k + \tilde{a}_z\frac{\tau_k^2}{2} \right) \frac{z_r + v_z\tau_k}{R}.\end{aligned}\tag{58}$$

For ease of analysis, Rigling rewrites (58) as a cubic polynomial expression

$$\Delta\tilde{R}_r(\tau_k) \approx -2(\tilde{\beta}_0 + \tilde{\beta}_1\tau_k + \tilde{\beta}_2\tau_k^2 + \tilde{\beta}_3\tau_k^3)\tag{59}$$

where the error terms are defined as

$$\tilde{\beta}_0 = \frac{\tilde{p}_x x_r + \tilde{p}_y y_r + \tilde{p}_z z_r}{R}\tag{60}$$

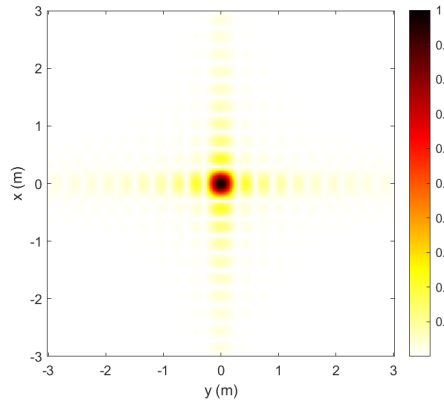
$$\tilde{\beta}_1 = \frac{\tilde{p}_x v_x + \tilde{p}_y v_y + \tilde{p}_z v_z + \tilde{v}_x x_r + \tilde{v}_y y_r + \tilde{v}_z z_r}{R}\tag{61}$$

$$\tilde{\beta}_2 = \frac{\tilde{v}_x v_x + \tilde{v}_y v_y + \tilde{v}_z v_z}{R} + \frac{\tilde{a}_x x_r + \tilde{a}_y y_r + \tilde{a}_z z_r}{2R}\tag{62}$$

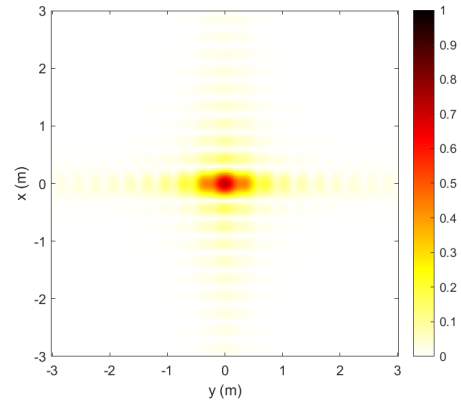
$$\tilde{\beta}_3 = \frac{\tilde{a}_x v_x + \tilde{a}_y v_y + \tilde{a}_z v_z}{2R}.\tag{63}$$

The separation of terms provides a clear indication of how MMEs are directly linked to constant, linear, quadratic, and cubic phase errors, which have varying effects on SAR image quality. The dominant effect of constant and linear phase errors is a spatially invariant shift in the imaged scatterer locations, while quadratic and cubic errors cause a “smeared” response in the final image. Examples of such smearing can be seen in Figures 5 and 6, and demonstrate the potential visual effects such errors can have on image quality.

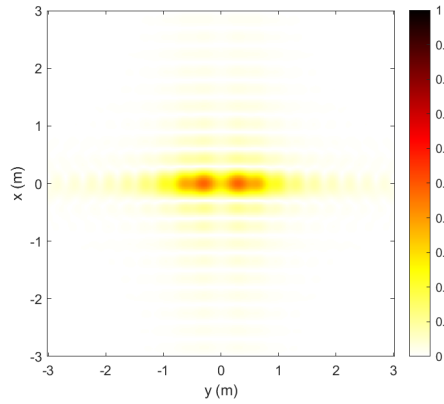




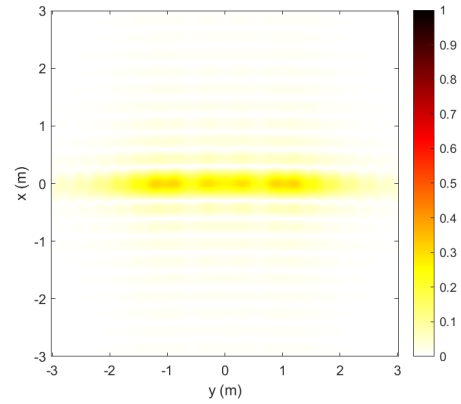
(a) No Velocity Error



(b) Velocity Error of 0.25 m/s

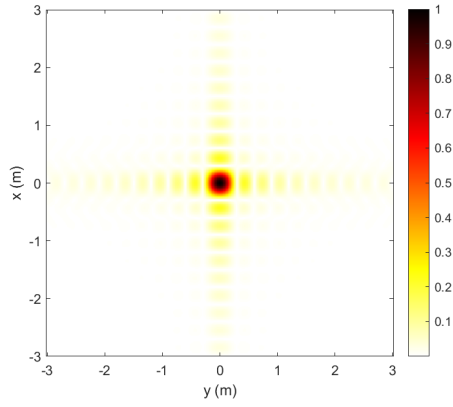


(c) Velocity Error of 0.50 m/s

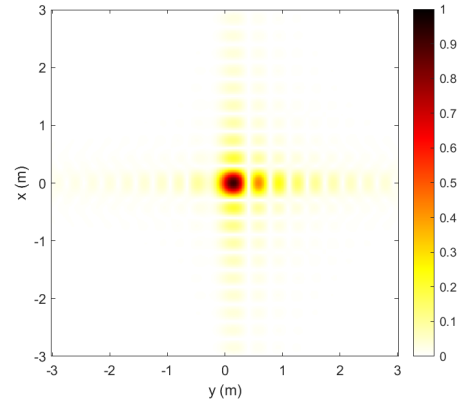


(d) Velocity Error of 1.00 m/s

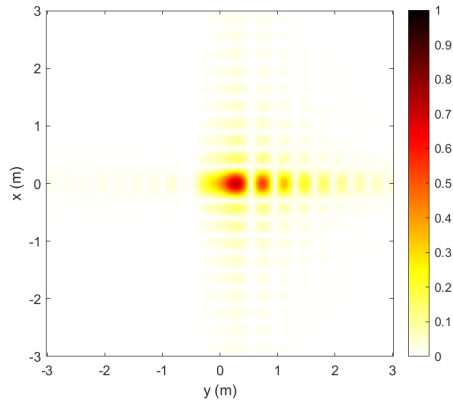
Figure 5: Effects of Various Along-Track Velocity Errors on SAR Image with Point Scatterer at (0,0)



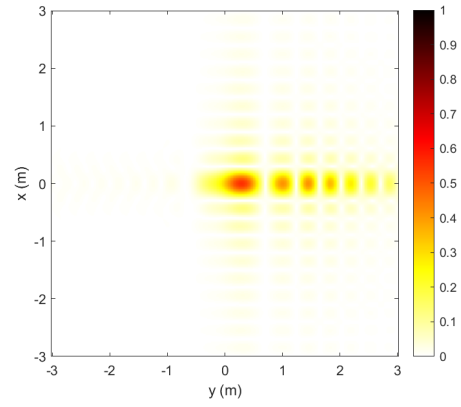
(a) No Acceleration Error



(b) Acceleration Error of  $0.5 \text{ m/s}^2$



(c) Acceleration Error of  $1.0 \text{ m/s}^2$



(d) Acceleration Error of  $2.0 \text{ m/s}^2$

Figure 6: Effects of Various Along-Track Acceleration Errors

Hence, the MMEs can be modeled in the spatial frequency domain by combining (28) and (59), such that

$$G_\epsilon(X, Y, Z) = e^{-jX_{ik}\left(\tilde{p}_x + \tilde{v}_x\tau_k + \frac{\tilde{a}_x\tau_k^2}{2}\right) + Y_{ik}\left(\tilde{p}_y + \tilde{v}_y\tau_k + \frac{\tilde{a}_y\tau_k^2}{2}\right) + Z_{ik}\left(\tilde{p}_z + \tilde{v}_z\tau_k + \frac{\tilde{a}_z\tau_k^2}{2}\right)} \quad (64)$$

$$= e^{jU_i\Delta\tilde{R}_r(\tau_k)/2} \quad (65)$$

$$= e^{-jU_i(\tilde{\beta}_0 + \tilde{\beta}_1\tau_k + \tilde{\beta}_2\tau_k^2 + \tilde{\beta}_3\tau_k^3)}. \quad (66)$$

Meanwhile, the phase terms can also be multiplied out for the true differential range in (55), as

$$\Delta R_m(\tau_k) \approx -2 \frac{x_m x_r + x_m v_x \tau_k + y_m y_r + y_m v_y \tau_k + z_m z_r + z_m v_z \tau_k}{R} \quad (67)$$

$$\approx -2 \left( \frac{x_m x_r + y_m y_r + z_m z_r}{R} \right) - 2 \left( \frac{x_m v_x + y_m v_y + z_m v_z}{R} \right) \tau_k \quad (68)$$

$$\approx -2(\beta_0 + \beta_1\tau_k). \quad (69)$$

Finally, (59) and (69) are combined into the differential range equation (52), so that

$$\Delta\hat{R}_m(\tau_k) = \Delta R_m(\tau_k) + \Delta\tilde{R}_r(\tau_k) \quad (70)$$

$$\approx -2(\beta_0 + \beta_1\tau_k + \tilde{\beta}_0 + \tilde{\beta}_1\tau_k + \tilde{\beta}_2\tau_k^2 + \tilde{\beta}_3\tau_k^3) \quad (71)$$

$$\approx -2(\beta_0 + \tilde{\beta}_0) - 2(\beta_1 + \tilde{\beta}_1)\tau_k - 2\tilde{\beta}_2\tau_k^2 - 2\tilde{\beta}_3\tau_k^3. \quad (72)$$

## 2.2 Image Quality Metrics

IQMs not only provide quantitative indications of image quality improvement, but can also provide numerical estimates of the phase error to be corrected through autofocus. As such, researchers have proposed a large number of autofocus algorithms based on optimization of IQMs such as sharpness [16–21], contrast [22–25], and entropy [26, 27]. However, higher-order phase errors (quadratic and above) affect each

IQM and the resulting autofocused images in different manners; therefore, careful IQM selection may lend towards improving the success of radar tasks such as target detection. The IQMs of interest for this thesis are contrast, sharpness, and entropy.

### 2.2.1 Contrast

By definition, contrast metrics evaluate the difference in brightness between the light and dark areas of an image. A well-focused image will have darker dark areas (representing high energy scattering in this thesis) and brighter bright areas (representing low energy scattering), as higher-order phase errors tend to smear energy from dark regions into the bright ones. This metric can be calculated as the ratio of the standard deviation to the mean of the image amplitude, as follows [9, 28]:

$$C_1 = \frac{\sqrt{E([A(n_x, n_y) - E(A(n_x, n_y))]^2)}}{E(A(n_x, n_y))} \quad (73)$$

where  $A(n_x, n_y)$  is the image pixel amplitude and  $E(\cdot)$  is the spatial average operator

$$E(A(n_x, n_y)) = \frac{1}{N_x N_y} \sum_{n_x=1}^{N_x} \sum_{n_y=1}^{N_y} A(n_x, n_y). \quad (74)$$

An alternate contrast metric can be defined as [22, 28]

$$C_2 = \frac{\sqrt{E([I(n_x, n_y) - E(I(n_x, n_y))]^2)}}{E(I(n_x, n_y))} \quad (75)$$

where  $I(n_x, n_y)$  is the image pixel intensity (also referred to as power or magnitude-squared)

$$I(n_x, n_y) = |A(n_x, n_y)|^2. \quad (76)$$

### 2.2.2 Sharpness

Sharpness metrics typically employ a function of the image intensity that will emphasize high-energy areas and de-emphasize low-energy areas. Parseval's theorem states that the total image energy, computed as the 2-D sum over image intensity, will remain constant, independent of any defocusing due to phase errors. However, a 2-D sum over a higher order power of image intensity, such as amplitude cubed or intensity squared, provides sensitivity to the defocusing effects of azimuth phase errors. For the purpose of this thesis, intensity squared

$$S = \sum_{n_x=1}^{N_x} \sum_{n_y=1}^{N_y} I(n_x, n_y)^2 \quad (77)$$

will be utilized for the sharpness metric [9, 16].

### 2.2.3 Entropy

Like the sharpness metric, the entropy metric may also be classified as a higher order function of image intensity. Entropy is classically used to quantify energy dispersion. Viewing the image defocusing effect of phase errors as a type of energy dispersion implies that, in general, image entropy will increase as phase errors worsen. In order to calculate image entropy, the SAR image intensity is first normalized, such that

$$\bar{I}(n_x, n_y) = \frac{I(n_x, n_y)}{\sum_{n_x=1}^{N_x} \sum_{n_y=1}^{N_y} I(n_x, n_y)}. \quad (78)$$

Now the entropy function can be defined as [9, 27, 29]

$$E_1 = - \sum_{n_x=1}^{N_x} \sum_{n_y=1}^{N_y} \bar{I}(n_x, n_y) \ln \bar{I}(n_x, n_y). \quad (79)$$

An alternative entropy function utilizes the normalized magnitude image

$$\hat{A}(n_x, n_y) = \frac{|A(n_x, n_y)|}{\sum_{n_x=1}^{N_x} \sum_{n_y=1}^{N_y} |A(n_x, n_y)|} \quad (80)$$

and defines entropy as [30]

$$E_2 = \sum_{n_x=1}^{N_x} \sum_{n_y=1}^{N_y} \hat{I}(n_x, n_y) e^{1-\hat{I}(n_x, n_y)}. \quad (81)$$

### III. SAR Imaging Process and CFAR Detector Setup

#### 3.1 Overview

This chapter describes the algorithms used to simulate the SAR imaging process, as well as the setup of the detector algorithms employed in the Monte Carlo trials for target detection.

#### 3.2 Complete Phase History Model

In Chapter II, the SAR system's 2-D point spread function was modeled as

$$H(X, Y) = \text{rect}\left(\frac{X - X_c}{\Delta X}\right) \text{rect}\left(\frac{Y}{\Delta Y}\right), \quad (82)$$

the phase history of the scene reflectivity as

$$G(X, Y) = \sum_{m=1}^M A_m e^{-j(x_m X_{ik} + y_m Y_{ik})} \quad (83)$$

$$\approx \sum_{m=1}^M A_m e^{-jU_i(\beta_{0m} + \beta_{1m}\tau_k)} \quad (84)$$

where

$$\beta_{0m} = \frac{x_m x_r + y_m y_r}{R} \quad (85)$$

$$\beta_{1m} = \frac{x_m v_x + y_m v_y}{R}, \quad (86)$$

and the phase history of the motion measurement errors as

$$G_\epsilon(X, Y) \approx e^{-jX_{ik}\left(\tilde{p}_x + \tilde{v}_x \tau_k + \frac{\tilde{a}_x \tau_k^2}{2}\right) + Y_{ik}\left(\tilde{p}_y + \tilde{v}_y \tau_k + \frac{\tilde{a}_y \tau_k^2}{2}\right)} \quad (87)$$

$$\approx e^{jU_i \Delta \tilde{R}_r / 2} \approx e^{-jU_i(\tilde{\beta}_0 + \tilde{\beta}_1 \tau_k + \tilde{\beta}_2 \tau_k^2 + \tilde{\beta}_3 \tau_k^3)} \quad (88)$$

where

$$\tilde{\beta}_0 = \frac{\tilde{p}_x x_r + \tilde{p}_y y_r}{R} \quad (89)$$

$$\tilde{\beta}_1 = \frac{\tilde{p}_x v_x + \tilde{p}_y v_y + \tilde{v}_x x_r + \tilde{v}_y y_r}{R} \quad (90)$$

$$\tilde{\beta}_2 = \frac{\tilde{v}_x v_x + \tilde{v}_y v_y}{R} + \frac{\tilde{a}_x x_r + \tilde{a}_y y_r}{2R} \quad (91)$$

$$\tilde{\beta}_3 = \frac{\tilde{a}_x v_x + \tilde{a}_y v_y}{2R}. \quad (92)$$

Through multiplication of the spatial frequency domain representation of the point spread function, the scene reflectivity, and the motion measurement errors, a complete model of the phase history data is formed as

$$R(X, Y) = G(X, Y)G_\epsilon(X, Y)H(X, Y) \quad (93)$$

$$\begin{aligned} &\approx \text{rect}\left(\frac{X - X_c}{\Delta X}\right) \text{rect}\left(\frac{Y}{\Delta Y}\right) \\ &\quad \sum_{m=1}^M A_m e^{-jX_{ik}\left(x_m + \tilde{p}_x + \tilde{v}_x \tau_k + \frac{\tilde{a}_x \tau_k^2}{2}\right) - jY_{ik}\left(y_m + \tilde{p}_y + \tilde{v}_y \tau_k + \frac{\tilde{a}_y \tau_k^2}{2}\right)} \end{aligned} \quad (94)$$

$$\approx \text{rect}\left(\frac{X - X_c}{\Delta X}\right) \text{rect}\left(\frac{Y}{\Delta Y}\right) \sum_{m=1}^M A_m e^{-jU_i(\beta_0 + \tilde{\beta}_0 + \beta_1 \tau_k + \tilde{\beta}_1 \tau_k + \tilde{\beta}_2 \tau_k^2 + \tilde{\beta}_3 \tau_k^3)}. \quad (95)$$

The inverse Fourier transform of the phase history data  $R(X, Y)$  provides a complete SAR estimate of the scene reflectivity:

$$r(x, y) = h(x, y) * g(x, y) * g_\epsilon(x, y) \quad (96)$$



where

$$h(x, y) * g(x, y) = \sum_{m=1}^M A_m \delta(x - x_m, y - y_m) * \frac{4\pi^2 e^{jX_c x}}{\rho_x \rho_y} \text{sinc}\left(\frac{x}{\rho_x}\right) \text{sinc}\left(\frac{y}{\rho_y}\right) \quad (97)$$

$$= \frac{4\pi^2}{\rho_x \rho_y} \sum_{m=1}^M A_m e^{jX_c(x-x_m)} \text{sinc}\left(\frac{x-x_m}{\rho_x}\right) \text{sinc}\left(\frac{y-y_m}{\rho_y}\right). \quad (98)$$

The motion measurement error  $g_\epsilon(x, y)$  portion of the scene reflectivity equation (96) is left here without a closed-form solution, as analytically solving the inverse Fourier transform of (87) has proven to be a very difficult task. Therefore, MMEs shall be represented simply as the inverse Fourier transform of  $G_\epsilon(X, Y)$ , leading to a full scene reflectivity model of

$$r(x, y) = h(x, y) * g(x, y) * g_\epsilon(x, y) \quad (99)$$

$$= \mathcal{F}^{-1}[G_\epsilon(X, Y)] * \frac{4\pi^2}{\rho_x \rho_y} \sum_{m=1}^M A_m e^{jX_c(x-x_m)} \text{sinc}\left(\frac{x-x_m}{\rho_x}\right) \text{sinc}\left(\frac{y-y_m}{\rho_y}\right). \quad (100)$$

### 3.3 SAR Image Grid

The fast-time variable  $t$  has been discussed as a continuous variable in order to facilitate explanation of the fundamental principles behind the phase history model derived in previous sections. However, in reality, the SAR processor samples the received signal using analog-to-digital converters (ADC), transforming fast time data  $t$  into discrete phase history data [8,9]. This data must then be appropriately interpolated onto a grid sized for display, which is accomplished in this thesis through PFA as discussed in Section 2.1.4. The end result is an image grid spaced in increments of  $dx$  and  $dy$  along the x- and y-axes, and numbering the pixels within this grid as  $n_x$  and  $n_y$ ; these two components combined effectively translate into coordinates to

pixel centers throughout the grid, represented by  $x' = n_x dx$  and  $y' = n_y dy$ . The SAR image model then becomes

$$r(x, y) = A(x', y') \quad (101)$$

$$= \mathcal{F}^{-1}[G_\epsilon(X, Y)] * \frac{4\pi^2}{\rho_x \rho_y} \sum_{m=1}^M A_m e^{j4\pi(x'-x_m)/\lambda} \text{sinc}\left(\frac{x'-x_m}{\rho_x}\right) \text{sinc}\left(\frac{y'-y_m}{\rho_y}\right) \quad (102)$$

where  $A(x', y')$  is the complex value of the pixel centered at  $(x', y')$ . From this point on in this thesis, the image pixel value will be denoted as  $A_n$ , to shorten it from  $A(x', y')$  but still differentiate it from target reflectivity complex amplitude  $A_m$ . Also, the constant factor of  $\frac{4\pi^2}{\rho_x \rho_y}$  is normalized out to simplify calculations, leaving

$$A_n = \mathcal{F}^{-1}[G_\epsilon(X, Y)] * \sum_{m=1}^M A_m e^{j4\pi(x'-x_m)/\lambda} \text{sinc}\left(\frac{x'-x_m}{\rho_x}\right) \text{sinc}\left(\frac{y'-y_m}{\rho_y}\right). \quad (103)$$

### 3.4 Statistics of a Pixel

In Section 3.3, it is shown that the process of transferring SAR data onto an imaging grid may lead to a deterministic scaling of reflected signal amplitudes; this scaling is not representative of a point scatterer's true reflectivity amplitude  $A_m$ , due to the imaging of the point scatterer at a location  $(x_m, y_m)$  that may not fall directly upon a corresponding pixel center  $(x', y')$ . In such cases, some of the point scatterer's representative reflective energy is shared with neighboring pixels. In addition, the sidelobes from the point scatterers representing clutter contribute additional amplitude to all other image pixel amplitudes. However, the mean and variance of the random pixel amplitudes can be accurately calculated using (101) with *a priori* knowledge of the range/crossrange resolutions and the image pixel dimensions to model the pixel amplitude probability distribution function.

The  $m$ th scatterer's complex random reflectivity amplitude  $A_m$  is computed in this thesis as the summation of random real and imaginary components  $u$  and  $v$ , both drawn from independent (and identical) zero-mean Gaussian distributions and each possessing exactly half of the reflective power, equating to a variance of  $\frac{\sigma_m^2}{2}$ , such that  $u_m \sim \mathcal{N}(0, \frac{\sigma_m^2}{2})$ ,  $v_m \sim \mathcal{N}(0, \frac{\sigma_m^2}{2})$ , and  $A_m = u_m + jv_m$ . The mean, variance, and second moment of the complex random amplitude are

$$\mathbb{E}[A_m] = \mathbb{E}[u_m + jv_m] = \mathbb{E}[u_m] + j\mathbb{E}[v_m] = 0 + j0 \quad (104)$$

$$\begin{aligned} \text{var}[A_m] &= \mathbb{E}[(A_m - \mathbb{E}[A_m])^2] \\ &= \mathbb{E}[(u_m + jv_m)^2] \\ &= \mathbb{E}[u_m^2 + j2u_mv_m + v_m^2] \\ &= \frac{\sigma_m^2}{2} + \mathbb{E}[u]^2 + j2\mathbb{E}[u]\mathbb{E}[v] + \frac{\sigma_m^2}{2} + \mathbb{E}[v]^2 \\ &= \sigma_m^2 \end{aligned} \quad (105)$$

$$\mathbb{E}[A_m^2] = \mathbb{E}[A_m]^2 + \text{var}[A_m] = 0^2 + \sigma_m^2 = \sigma_m^2 \quad (106)$$

Meanwhile, taking the magnitude of the two components' sum leads to  $|A_m| = \sqrt{u_m^2 + v_m^2}$ . The square root of the sum of squares of two i.i.d. zero-mean Gaussian random variables with the same variance exhibits a Rayleigh distribution [31], such that  $|A_m| \sim \text{Rayleigh}(\frac{\sigma_m}{\sqrt{2}})$ ; therefore, the expected value, variance, and second moment of  $|A_m|$  are [32]

$$\mathbb{E}[|A_m|] = \sqrt{\frac{\pi\sigma_m^2}{4}} = \frac{\sigma_m\sqrt{\pi}}{2} \quad (107)$$

$$\text{Var}[|A_m|] = \sigma_m^2 - \frac{\pi\sigma_m^2}{4} = \sigma_m^2 \left(1 - \frac{\pi}{4}\right) \quad (108)$$

$$\mathbb{E}[|A_m|^2] = \mathbb{E}[A_m^2] = \sigma_m^2. \quad (109)$$

Equation (101) shows that, after the scene reflectivity data has gone through

image processing,  $A_m$  is modified by a scale factor that is dependent on point scatterer location  $(x_m, y_m)$  in relation to pixel centers  $(x', y')$ , as well as phase. This scaling factor is represented as  $\eta_m$ , such that

$$\eta_m = e^{j4\pi(x'-x_m)/\lambda} \text{sinc}\left(\frac{x'-x_m}{\rho_x}\right) \text{sinc}\left(\frac{y'-y_m}{\rho_y}\right) \quad (110)$$

Without motion measurement errors, the pixel amplitude can now be modeled as

$$A_n = \sum_{m=1}^M \eta_m A_m \quad (111)$$

whereas it is

$$A_n = g_\epsilon(x, y) * \sum_{m=1}^M \eta_m A_m \quad (112)$$

when affected by MMEs.

The scale factor  $\eta_m$  is essentially a linear transform on the complex Gaussian random variable  $A_m$ , for which the scaling results in another complex Gaussian random variable that can again be fully described by its mean and variance. Because the scale factor  $\eta_m$  itself is not random, its expected value is equal to the factor itself ( $E[\eta_m] = \eta_m$ ) and does not vary ( $\text{Var}[\eta_m] = 0$ ). Hence, the expected value for each error-free pixel amplitude is

$$E[A_n] = E\left[\sum_{m=1}^M \eta_m A_m\right] \quad (113)$$

$$= \sum_{m=1}^M E[\eta_m(u_m + jv_m)] \quad (114)$$

$$= \sum_{m=1}^M \eta_m(E[u] + jE[v]) \quad (115)$$

$$= 0 + j0 \quad (116)$$

and the variance is

$$\text{Var}[A_n] = \text{Var} \left[ \sum_{m=1}^M \eta_m A_m \right] \quad (117)$$

$$= \text{E} \left[ \left( \sum_{m=1}^M \eta_m A_m - E \left[ \sum_{m=1}^M \eta_m A_m \right] \right)^2 \right] \quad (118)$$

$$= \text{E} \left[ \left( \sum_{m=1}^M \eta_m A_m \right)^2 \right] \quad (119)$$

$$= \text{E} \left[ \sum_{m=1}^M \eta_m^2 A_m^2 + \sum_{m \neq j}^M \eta_m \eta_j A_m A_j \right] \quad (120)$$

$$= \sum_{m=1}^M \eta_m^2 \text{E}[A_m^2] + \sum_{m \neq j}^M \eta_m \eta_j \text{E}[A_m A_j] \quad (121)$$

$$= \sum_{m=1}^M \eta_m^2 \sigma_m^2. \quad (122)$$

The statistics derived here only apply to pixels unaffected by MMEs. Due to the difficulty of deriving an analytic solution for the MME model  $g_\epsilon(x, y)$ , this thesis relies on numerical analysis of the pixel amplitudes when they have been altered by MMEs.

### 3.5 Target Detection

In order to perform target detection on a SAR image, it would be ideal to set up a likelihood ratio test (LRT) expressed as

$$\Lambda_{LRT}(A_n) = \frac{p(A_n|H_1)}{p(A_n|H_0)} \underset{H_0}{\overset{H_1}{\geq}} \frac{P(H_0)}{P(H_1)} \quad (123)$$

where hypothesis  $H_1$  represents the presence of a target (as well as clutter), whereas  $H_0$  represents the sole presence of clutter. However, utilization of an LRT for SAR detection would require *a priori* knowledge of the probability densities for each hypothesis ( $P(H_1)$  and  $P(H_0)$ ), which is not likely to be known for an operational SAR

system. Instead, a NP detector [32] can be implemented such that

$$\Lambda_{NP}(A_n) = \frac{p(A_n|H_1)}{p(A_n|H_0)} \underset{H_0}{\overset{H_1}{\gtrless}} \gamma. \quad (124)$$

With the NP detector, only the likelihood of encountering a particular pixel amplitude  $A_n$  within each hypothesis region ( $p(A_n|H_1)$  and  $p(A_n|H_0)$ ) must be known. The resultant ratio can then be evaluated against a detection threshold  $\gamma$  which is set to maximize probability of detection ( $P_D$ ) while maintaining a desired probability of false alarm ( $P_{FA}$ ). Setting a constant false alarm rate in this manner is referred to as CFAR detection, where the constant false alarm rate is expressed as

$$P_{FA} = \int_{A_n: \Lambda > \gamma} p(A_n|H_0) dA_n \quad (125)$$

CFAR detection is one of the most popular detection algorithms used on SAR imagery [33], but it requires accurate modeling of pixel probability densities for both clutter and targets. While literature presents a fairly large number of realistic distribution models for clutter, including log-normal, Weibull, gamma, and K-distributions [34], the clutter (and target) pixel magnitudes are modeled in this thesis with a Rayleigh distribution derived from complex Gaussian point scatterer reflectivities. The use of complex Gaussian distributions facilitates derivation of the necessary test statistics.

The image pixel probability density is derived by first focusing on scatterer reflectivity as represented in the point scatterer model. The real and imaginary components  $u_m$  and  $v_m$  of scatterer reflectivity amplitudes  $A_m$  are separated into two vectors, such that  $\mathbf{u} = [u_1, u_2, \dots, u_M]^T$  and  $\mathbf{v} = [v_1, v_2, \dots, v_M]^T$ , respectively, for a quantity of  $M$  scatterers. The two component vectors  $\mathbf{u}$  and  $\mathbf{v}$  are then stacked into a single

$2M$ -length real random vector  $\mathbf{A}$ , such that

$$\mathbf{A} = \begin{bmatrix} \mathbf{u} \\ \mathbf{v} \end{bmatrix} = [u_1, u_2, \dots, u_M, v_1, v_2, \dots, v_M]^T \quad (126)$$

Section 3.4 states that the independent and identical components  $u$  and  $v$  each follow a zero-mean Gaussian distribution and possess a variance of  $\frac{\sigma_m^2}{2}$ ; therefore, the expected value of  $\mathbf{A}$  is defined as

$$\mathbb{E}[\mathbf{A}] = \boldsymbol{\mu} = \mathbb{E} \begin{bmatrix} \mathbf{u} \\ \mathbf{v} \end{bmatrix} = \begin{bmatrix} \boldsymbol{\mu}_u \\ \boldsymbol{\mu}_v \end{bmatrix} = \mathbf{0} \quad (127)$$

and the covariance matrix as

$$\boldsymbol{\Sigma} = \mathbb{E}[(\mathbf{A} - \mathbb{E}[\mathbf{A}])(\mathbf{A} - \mathbb{E}[\mathbf{A}])^T] \quad (128)$$

$$= \mathbb{E}[(\mathbf{A} - \boldsymbol{\mu}_A)(\mathbf{A} - \boldsymbol{\mu}_A)^T] \quad (129)$$

$$= \mathbb{E}[\mathbf{A}\mathbf{A}^T] - \boldsymbol{\mu}_A\boldsymbol{\mu}_A^T \quad (130)$$

$$= \begin{bmatrix} \boldsymbol{\Sigma}_{uu} & \boldsymbol{\Sigma}_{uv} \\ \boldsymbol{\Sigma}_{vu} & \boldsymbol{\Sigma}_{vv} \end{bmatrix} \quad (131)$$

where

$$\boldsymbol{\Sigma}_{uu} = \begin{bmatrix} \text{var}(u_1) & \text{cov}(u_1, u_2) & \dots & \text{cov}(u_1, u_M) \\ \text{cov}(u_2, u_1) & \text{var}(u_2) & \dots & \text{cov}(u_2, u_M) \\ \vdots & \vdots & \ddots & \vdots \\ \text{cov}(u_M, u_1) & \text{cov}(u_M, u_2) & \dots & \text{var}(u_M) \end{bmatrix} = \begin{bmatrix} \frac{\sigma_1^2}{2} & 0 & \dots & 0 \\ 0 & \frac{\sigma_2^2}{2} & \dots & 0 \\ \vdots & \vdots & \ddots & \vdots \\ 0 & 0 & \dots & \frac{\sigma_M^2}{2} \end{bmatrix} = \boldsymbol{\Sigma}_{vv} \quad (132)$$

$$\boldsymbol{\Sigma}_{uv} = -\boldsymbol{\Sigma}_{vu} = \mathbf{0} \quad (133)$$

The point scatterer reflectivity vector is now fully characterized as multi-dimensional Gaussian  $\mathbf{A} \sim \mathcal{N}(\mathbf{0}, \mathbf{\Sigma})$ ; however, the CFAR detector still needs the probability density of pixel measurement  $A_n$  in order to function. Noting that the pixel amplitude is simply the scaled sum of target reflectivity amplitudes ( $A_n = \sum_{m=1}^M \eta_m A_m$ ), the scale factor  $\eta_m$  can be separated into its real and imaginary components, in the same manner that the reflectivity amplitude was separated into two components. These components are represented as

$$\eta_{rm} = \text{Re}\{e^{j4\pi(x'-x_m)/\lambda}\} \text{sinc}\left(\frac{x' - x_m}{\rho_x}\right) \text{sinc}\left(\frac{y' - y_m}{\rho_y}\right) \quad (134)$$

$$\eta_{im} = \text{Im}\{e^{j4\pi(x'-x_m)/\lambda}\} \text{sinc}\left(\frac{x' - x_m}{\rho_x}\right) \text{sinc}\left(\frac{y' - y_m}{\rho_y}\right) \quad (135)$$

Two scaling vectors are generated from the components, where  $\mathbf{N}_r = [\eta_{r1}, \eta_{r2}, \dots, \eta_{rM}]^T$  and  $\mathbf{N}_i = [\eta_{i1}, \eta_{i2}, \dots, \eta_{iM}]^T$ . The new vectors are used to scale the stacked  $\mathbf{u}$  and  $\mathbf{v}$  vectors to create stacked pixel measurement vector  $\mathbf{A}_n$ , such that

$$\mathbf{A}_n = \begin{bmatrix} u_n \\ v_n \end{bmatrix} = \begin{bmatrix} \mathbf{N}_r^T \mathbf{u} \\ \mathbf{N}_i^T \mathbf{v} \end{bmatrix} = \begin{bmatrix} \sum_{m=1}^M \eta_{rm} u_m \\ \sum_{m=1}^M \eta_{im} v_m \end{bmatrix} \quad (136)$$

where  $u_n$  and  $v_n$  are the real and imaginary components of the complex pixel measurement  $A_n$ . This new pixel vector, which consists of scaled Gaussian components and is therefore Gaussian itself, assists in deriving the mean and covariance matrices of the pixel amplitude:

$$\boldsymbol{\mu}_n = \text{E}[\mathbf{A}_n] = \text{E} \begin{bmatrix} u_n \\ v_n \end{bmatrix} = \text{E} \begin{bmatrix} \mathbf{N}_r^T \mathbf{u} \\ \mathbf{N}_i^T \mathbf{v} \end{bmatrix} = \begin{bmatrix} \mathbf{N}_r^T \boldsymbol{\mu}_u \\ \mathbf{N}_i^T \boldsymbol{\mu}_v \end{bmatrix} = \mathbf{0} \quad (137)$$



$$\mathbf{\Sigma}_n = \text{E}[(\mathbf{A}_n - \text{E}[\mathbf{A}_n])(\mathbf{A}_n - \text{E}[\mathbf{A}_n])^T] \quad (138)$$

$$= \text{E}[\mathbf{A}_n \mathbf{A}_n^T] - \boldsymbol{\mu}_n \boldsymbol{\mu}_n^T \quad (139)$$

$$= \text{E} \left[ \begin{bmatrix} \mathbf{N}_r^T \mathbf{u} \\ \mathbf{N}_i^T \mathbf{v} \end{bmatrix} \begin{bmatrix} \mathbf{u}^T \mathbf{N}_r & \mathbf{v}^T \mathbf{N}_i \end{bmatrix} \right] \quad (140)$$

$$= \text{E} \begin{bmatrix} \mathbf{N}_r^T \mathbf{u} \mathbf{u}^T \mathbf{N}_r & \mathbf{N}_r^T \mathbf{u} \mathbf{v}^T \mathbf{N}_i \\ \mathbf{N}_i^T \mathbf{v} \mathbf{u}^T \mathbf{N}_r & \mathbf{N}_i^T \mathbf{v} \mathbf{v}^T \mathbf{N}_i \end{bmatrix} \quad (141)$$

$$= \text{E} \begin{bmatrix} \mathbf{N}_r^T \boldsymbol{\Sigma}_{uu} \mathbf{N}_r & \mathbf{N}_r^T \boldsymbol{\Sigma}_{uv} \mathbf{N}_i \\ \mathbf{N}_i^T \boldsymbol{\Sigma}_{vu} \mathbf{N}_r & \mathbf{N}_i^T \boldsymbol{\Sigma}_{vv} \mathbf{N}_i \end{bmatrix} \quad (142)$$

$$= \frac{1}{2} \begin{bmatrix} \sum_{m=1}^M \eta_{rm}^2 \sigma_m^2 & 0 \\ 0 & \sum_{m=1}^M \eta_{im}^2 \sigma_m^2 \end{bmatrix} \quad (143)$$

It is important to note that covariance matrix  $\mathbf{\Sigma}_n$  only relates the real and imaginary components of a single SAR pixel; it does **not** relate one pixel to another because SAR image pixels are not independent of each other and therefore would require a more complex covariance matrix to describe their relation. Equations (137) and (143) show that  $\boldsymbol{\mu}_n$  is a  $2 \times 1$  zero vector and  $\mathbf{\Sigma}_n$  is a  $2 \times 2$  scalar matrix; together, they fully characterize a single (bivariate Gaussian) SAR pixel as  $\mathbf{A}_n \sim \mathcal{N}(\mathbf{0}, \mathbf{\Sigma}_n)$ . This information can now be used to find the pixel's probability density:

$$p(\mathbf{A}_n) = \frac{e^{-\frac{1}{2}(\mathbf{A}_n - \boldsymbol{\mu}_n)^T \mathbf{\Sigma}_n^{-1} (\mathbf{A}_n - \boldsymbol{\mu}_n)}}{\sqrt{(2\pi)^2 |\mathbf{\Sigma}_n|}} = \frac{e^{-\frac{1}{2} \mathbf{A}_n^T \mathbf{\Sigma}_n^{-1} \mathbf{A}_n}}{2\pi \sqrt{|\mathbf{\Sigma}_n|}} \quad (144)$$

For target detection purposes, each SAR image pixel can be classified as either “target” or “clutter”. In this thesis, target pixels are defined as pixels containing point scatterers that possess a reflectivity variance of  $\sigma_t^2$ , while clutter pixels solely possess point scatterers with reflectivity variance of  $\sigma_c^2$ . The clutter reflectivity variance is assumed to remain constant throughout the entire target scene; this means that the

i.i.d. zero-mean Gaussian components  $u_c \sim \mathcal{N}(0, \frac{\sigma_c^2}{2})$  and  $v_c \sim \mathcal{N}(0, \frac{\sigma_c^2}{2})$  are equal, and re-deriving (127) to (144) leads to clutter pixel measurement vector  $\mathbf{A}_c \sim \mathcal{N}(\mathbf{0}, \mathbf{\Sigma}_c)$ , where

$$\mathbf{\Sigma}_c = \frac{\sigma_c^2}{2} \begin{bmatrix} \sum_{m=1}^M \eta_{rm}^2 & 0 \\ 0 & \sum_{m=1}^M \eta_{im}^2 \end{bmatrix} \quad (145)$$

For the sake of simplicity, all target point scatterers are also assumed to have equal reflectivity variance  $\sigma_t^2$ . This assumption results in target pixel covariance matrix  $\mathbf{\Sigma}_t$  where

$$\mathbf{\Sigma}_t = \frac{\sigma_t^2}{2} \begin{bmatrix} \sum_{m=1}^M \eta_{rm}^2 & 0 \\ 0 & \sum_{m=1}^M \eta_{im}^2 \end{bmatrix}. \quad (146)$$

The preceding image pixel information can now be used to properly set up the binary hypotheses to be utilized in the CFAR detector. The null hypothesis  $H_0$  will indicate a clutter pixel possessing solely point scatterers with reflectivity variance  $\sigma_c^2$ , as defined above; such a pixel's probability density would be described by a clutter pixel covariance matrix, so that  $p(\mathbf{A}_n|H_0) \sim \mathcal{N}(\mathbf{0}, \mathbf{\Sigma}_c)$ . Meanwhile, the alternative hypothesis  $H_1$  will indicate the target's presence (with variance  $\sigma_t^2$ ) within the evaluated pixel; however, the pixel would also potentially contain clutter as well, so the probability density of a target pixel would necessarily be described by clutter and target covariance matrices summed together, such that  $p(\mathbf{A}_n|H_1) \sim \mathcal{N}(\mathbf{0}, \mathbf{\Sigma}_t + \mathbf{\Sigma}_c)$ . Therefore, the requisite binary hypotheses take the following form:

$$H_0 : \mathbf{A}_n \sim \mathcal{N}(\mathbf{0}, \mathbf{\Sigma}_c) \quad (147)$$

$$H_1 : \mathbf{A}_n \sim \mathcal{N}(\mathbf{0}, \mathbf{\Sigma}_t + \mathbf{\Sigma}_c). \quad (148)$$

Utilizing the Neyman-Pearson criteria laid out in (124) and the joint distribution of

$\mathbf{A}_n$  found in (144), the LRT can now be defined as

$$\Lambda(\mathbf{A}_n) = \frac{p(\mathbf{A}_n|H_1)}{p(\mathbf{A}_n|H_0)} \quad (149)$$

$$= \frac{e^{-\frac{1}{2}\mathbf{A}_n^T(\boldsymbol{\Sigma}_t+\boldsymbol{\Sigma}_c)^{-1}\mathbf{A}_n} \sqrt{(2\pi)^2|\boldsymbol{\Sigma}_c|}}{\sqrt{(2\pi)^2|\boldsymbol{\Sigma}_t+\boldsymbol{\Sigma}_c|} e^{-\frac{1}{2}\mathbf{A}_n^T\boldsymbol{\Sigma}_c^{-1}\mathbf{A}_n}} \quad (150)$$

$$= \sqrt{\frac{|\boldsymbol{\Sigma}_c|}{|\boldsymbol{\Sigma}_t+\boldsymbol{\Sigma}_c|}} e^{-\frac{1}{2}\mathbf{A}_n^T[(\boldsymbol{\Sigma}_t+\boldsymbol{\Sigma}_c)^{-1}-\boldsymbol{\Sigma}_c^{-1}]\mathbf{A}_n} \underset{H_0}{\overset{H_1}{\gtrless}} \gamma \quad (151)$$

and the log-likelihood ratio is

$$\ln \Lambda(\mathbf{A}_n) = \frac{1}{2} \ln |\boldsymbol{\Sigma}_c| - \frac{1}{2} \ln |\boldsymbol{\Sigma}_t + \boldsymbol{\Sigma}_c| - \frac{1}{2} \mathbf{A}_n^T [(\boldsymbol{\Sigma}_t + \boldsymbol{\Sigma}_c)^{-1} - \boldsymbol{\Sigma}_c^{-1}] \mathbf{A}_n \underset{H_0}{\overset{H_1}{\gtrless}} \gamma' \quad (152)$$

where new threshold  $\gamma' = \ln \gamma$ . To find a suitable test statistic, the constant terms are moved into the threshold, leaving

$$T(\mathbf{A}_n) = -\frac{1}{2} \mathbf{A}_n^T [(\boldsymbol{\Sigma}_t + \boldsymbol{\Sigma}_c)^{-1} - \boldsymbol{\Sigma}_c^{-1}] \mathbf{A}_n \underset{H_0}{\overset{H_1}{\gtrless}} \gamma'. \quad (153)$$

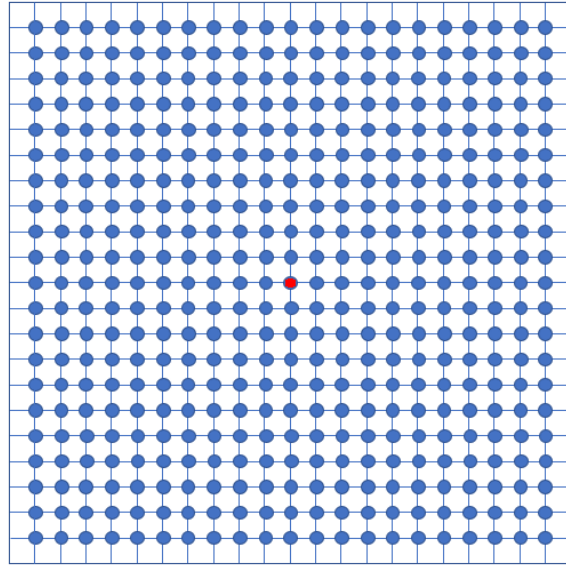


Figure 7: Plot of all simulated point scatterers; blue points represent clutter, and red point represents a target point scatterer stacked on top of a clutter point scatterer

As seen in (153), the test statistic relies on the complex pixel amplitude vector  $\mathbf{A}_n$ , as well as the target and clutter covariance matrices  $\Sigma_t$  and  $\Sigma_c$ . In order to calculate the values for these parameters, a target scene is set up with a scene extent  $D_x$  meters long in the range direction and  $D_y$  meters long in the cross-range direction. For this thesis, such a target scene possesses 441 clutter point scatterers are distributed evenly throughout the scene as shown in Figure 7. It is assumed that only one target scatterer is present in the target scene, and that it is always located in the very center of the scene; a target placed in such a manner would necessarily share the same space as the clutter point scatterer at the scene center, as also seen in Figure 7. Such stringent assumptions are set only because the purpose of the thesis is to compare IQMs to the task of target detection, not to encounter the best target detection algorithm.



Figure 8: Depiction of CFAR stencil used for target detection in this simulation.

Also necessary for test statistic calculation is the utilization of a sliding CFAR detector window. Figure 8 displays a CFAR stencil that is  $5 \times 5$  pixels in size; this stencil “slides” sequentially over each tested image pixel, or CUT. The CUT (shown in green) provides the measurements for the complex pixel amplitude and the target

covariance matrix, while the clutter covariance matrix is estimated using measurements gathered from the pixels within the background clutter band (in yellow). The two regions are separated by a guard band (in blue) to prevent incidental mixture of the two sets of measurements. The CUT can be comprised of either a single pixel or multiple pixels, but it is recommended that it be the size of the smallest expected target, while the size of the guard band should be large enough to encompass the largest expected target [34]. In this thesis, all SAR image pixels are resolution-sized, as is typical for PFA-formed images; therefore, the target is the size of a single pixel, and only a single-pixel CUT is necessary. This assumption leads to a target covariance matrix  $\Sigma_t$  that is equivalent to identity matrix  $\mathbf{I}$ . Meanwhile, the clutter covariance matrix  $\Sigma_c$  is estimated utilizing a sample covariance matrix  $\hat{\Sigma}_c$  that is determined as

$$\hat{\Sigma}_c = \frac{1}{j-1} \sum_{i=1}^j (\mathbf{A}_i - \bar{\mathbf{A}}_c)(\mathbf{A}_i - \bar{\mathbf{A}}_c)^T \quad (154)$$

where  $j$  is the number of pixels utilized to form the sample (i.e., the number of pixels in the background clutter band);  $\mathbf{A}_i$  is the pixel measurement vector of the  $i$ th clutter pixel under consideration, similar in structure to the pixel measurement vector  $\mathbf{A}_n$  as expressed in (136); and  $\bar{\mathbf{A}}_c$  is the sample mean of all  $j$  pixel measurement vectors, as evaluated in

$$\bar{\mathbf{A}}_c = \frac{1}{j} \sum_{i=1}^j \mathbf{A}_i \quad (155)$$

Thus, the  $2 \times 2$  sample covariance matrix  $\hat{\Sigma}_c$ , relating the real and imaginary parts of a single pixel, is approximated by spatially averaging over the sample means and  $2 \times 2$  covariances of the pixels in the background region of the CFAR window. Because the background region always possesses sixteen pixels ( $j = 16$ ), the sample mean vector

and sample covariance matrix ultimately become

$$\bar{\mathbf{A}}_c = \frac{1}{16} \sum_{i=1}^{16} \mathbf{A}_i \quad (156)$$

$$\hat{\Sigma}_c = \frac{1}{15} \sum_{i=1}^{16} (\mathbf{A}_i - \bar{\mathbf{A}}_c)(\mathbf{A}_i - \bar{\mathbf{A}}_c)^T \quad (157)$$

and the test statistic employed for target detection in this thesis becomes

$$T(\mathbf{A}_n) = \frac{1}{2} \mathbf{A}_n^T [\hat{\Sigma}_c^{-1} - (\mathbf{I} + \hat{\Sigma}_c)^{-1}] \mathbf{A}_n \underset{H_1}{\overset{H_0}{\geq}} \gamma'. \quad (158)$$

The test statistic portrayed in (158) would work well on SAR images gained through precisely-measured platform motion; however, the lack of motion measurement errors would be considered an unrealistic scenario for true SAR observations. Unfortunately, difficulties in arriving at a closed-form solution for the addition of MMEs forces a numerical review of the results.

### 3.6 Number of Required Monte Carlo Trials

To ensure accuracy in the results and findings, a requirement is set such that the randomized reflectivity amplitudes  $A_m$  are accurate to within  $\pm 0.1$  units 95% of the time; this requirement subsequently forces a certain level of pixel amplitude accuracy as well. Since the reflectivity amplitudes are all i.i.d., the central limit theorem is invoked; this theorem states that as a number of samples approaches infinity, the sample mean is normal distributed regardless of the type of data distribution from which the samples were taken. Kay prescribes the following equation for finding the probability that a certain quantity exceeds a specific amount of error  $\epsilon$  [32]:

$$\Pr[T > \epsilon] = Q\left(\frac{\epsilon}{\sqrt{\sigma^2/N}}\right) \quad (159)$$

where  $\sigma_m$  is the standard deviation of reflectivity amplitudes  $A_m$  and  $N$  is the number of realizations needed to achieve a confidence level equal to  $100(1 - \alpha)\%$ . The probability found in (159) will be equal to half the margin of error  $\alpha$ , so substituting  $\Pr[T > \epsilon] = \alpha/2$  results in

$$N \geq \left( \frac{\sigma_m Q^{-1}(\alpha/2)}{\epsilon} \right)^2, \quad (160)$$

with which the minimum number of realizations needed can now be determined for the differing values of  $\sigma_m$  utilized in this simulation, as listed in Table 1.

Table 1: Minimum number of realizations needed for different standards of deviation at 95% confidence in  $\pm 0.1$  amplitude error

$\sigma_m$	$N$ realizations
1	384
2	1537
3	3458
4	6147
5	9604

Table 1 shows that at least 9604 realizations would be needed to attain the desired level of confidence in an amplitude error of  $\pm 0.1$  when the target amplitude reaches the largest assigned standard deviation of 5. As such, the simulation will utilize 10000 realizations of all SAR images and related artifacts, in order to maintain a 95%-or-higher level of confidence in not exceeding a margin of 0.1 units of reflectivity amplitude.

## IV. Results and Analysis

### 4.1 Overview

This chapter covers the effects of implementing various motion measurement errors on target detection within simulated SAR images of different signal-to-clutter ratios. It also examines the image quality levels achieved after MME implementation, and compares these metrics to achieved probabilities of detection.

### 4.2 Simulation Setup

Table 2: SAR Simulation Parameters

SAR Image Parameters	Symbol	Values
Scene Extent (m)	$D_x, D_y$	$6.0 \times 6.0$
Pixel Size (m)	$dx, dy$	$0.3 \times 0.3$
Range and Cross-Range Resolution (m)	$\rho_x, \rho_y$	$0.3 \times 0.3$
Frequency Range (GHz)	$f$	$\in [8.7502, 9.2498]$
Bandwidth (MHz)	$\Delta f$	499.65
Frequency Sample Spacing (MHz)	$\delta f$	0.9993
Azimuth Range (deg)	$\phi$	$\in [-1.5907, 1.5907]$
Azimuth Extent (deg)	$\Delta \phi$	3.1813
Azimuth Sample Spacing (deg)	$\delta \phi$	0.063626
Grazing Angle (deg)	$\psi$	0

As previously described in Section 3.5 and shown in Table 2, a  $6 \times 6$ -meter scene is simulated with 144 clutter point scatterers and one target point scatterer. Data collection is simulated using a frequency range of 8.75-9.25 GHz for a center frequency of 9 GHz and a bandwidth of 499.65 MHz, and a transmit aperture extending from  $-1.59^\circ$  to  $1.59^\circ$  for an azimuth extent of  $3.18^\circ$ ; these parameters result in both a ground range resolution  $\rho_x$  and a ground cross-range resolution of 0.3 meters. The pixel size of the image grid is purposely set to  $0.3 \times 0.3$ -m as well, allowing each clutter scatterer to appear in the exact center of each image pixel.



As indicated in previous sections, the generation of all point scatterers into phase history is accomplished by drawing the complex reflectivity amplitudes  $A_m$  for both clutter and target from Gaussian random processes with means of zero and variances of  $\frac{\sigma_c^2}{2}$  and  $\frac{\sigma_t^2}{2}$ , respectively. In order to further enhance potential trends and comparisons between MMEs, IQMs, and target detection, five different sets of target scenes are incorporated into the simulation, corresponding to five different SCRs: 1, 4, 9, 16, and 25. These five SCRs are chosen for test variety as well as simplified implementation, as they are easily achieved by maintaining a static clutter reflectivity variance  $\sigma_c^2$  of 1, while increasing the target reflectivity standard deviation  $\sigma_t$  in unit steps from 1 to 5 (understanding that the ratio  $\sigma_t^2/\sigma_c^2$  has equivalency to SCR). Then 10000 realizations are produced for each SCR scenario, resulting in 50000 unique SAR phase histories. The Polar Reformatting Algorithm, as described in Section 2.1.4, is applied to the phase history data to produce 10000 SAR images for each SCR set, 50000 in total.

Table 3: Theoretical vs Simulated Target Reflectivity Amplitude Statistics

SCR	$A_m$ Mean		$A_m$ Variance	
	Theoretical	Simulated	Theoretical	Simulated
25	0+j0	-0.0193 + j0.1205	25	25.090
16	0+j0	-0.0154 + j0.0964	16	16.057
9	0+j0	-0.0115 + j0.0723	9	9.0323
4	0+j0	-0.0077 + j0.0482	4	4.0144
1	0+j0	-0.0038 + j0.0241	1	1.0036

For validation of correct implementation of the necessary phase histories, statistics are tabulated for each set of SCRs and compared to what is theoretically derived for (104) and (105) in Table 3. This table shows that the variances for all the target reflectivity amplitudes are within 0.1 units of the theoretical variances, as was intended with the high number of amplitude realizations.

To ensure correct formation of the related SAR images, statistics are compared

Table 4: Theoretical vs Simulated Target Pixel Statistics

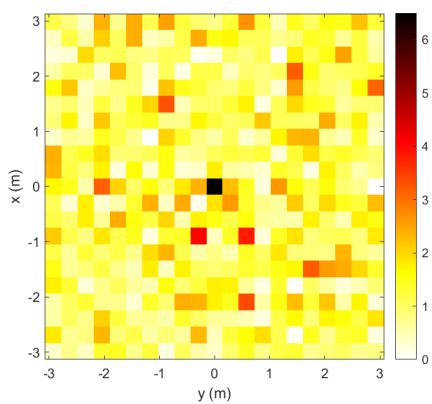
SCR	$A_n H_1$ Mean		$A_n H_1$ Variance	
	Theoretical	Simulated	Theoretical	Simulated
25	0+j0	-0.0027 + j0.0946	26	26.053
16	0+j0	0.0000 + j0.0776	17	17.028
9	0+j0	0.0027 + j0.0605	10	10.011
4	0+j0	0.0054 + j0.0435	5	5.0003
1	0+j0	0.0082 + j0.0264	2	1.9971

Table 5: Theoretical vs Simulated Clutter Pixel Statistics

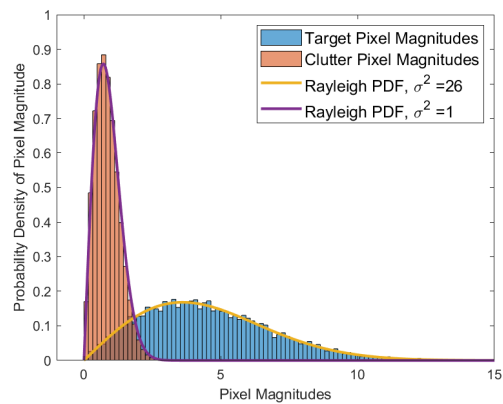
SCR	$A_n H_0$ Mean		$A_n H_0$ Variance	
	Theoretical	Simulated	Theoretical	Simulated
25	0+j0	0.0002 + j0.0000	1	0.9296
16	0+j0	0.0002 + j0.0000	1	0.9292
9	0+j0	0.0002 + j0.0000	1	0.9289
4	0+j0	0.0002 + j0.0000	1	0.9287
1	0+j0	0.0002 + j0.0000	1	0.9285

for both clutter and target pixels to what was theoretically derived in (116) and (122) over each set of SCRs in Tables 4 and 5. Here, the results again show that the measured variance of the simulated target pixels matches the theoretical pixel variance to within 0.1 units in all cases.

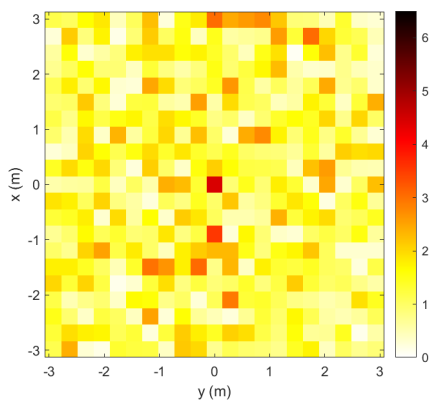
Figures 9a, 9c, and 9e depict sample SAR images using differing SCRs, while the histograms in Figures 9b, 9d, and 9f display the simulated magnitude distributions of the target and clutter pixels; target pixels are represented by the blue bars, and the clutter pixels are shown as red bars. The colored lines drawn over the histograms represent the calculated theoretical probability density function for the pixel magnitudes in images with the specified SCR to demonstrate the validity of each particular set of 10000 SAR images. Figure 9a displays a sample SAR image from the 10000 produced with an SCR of 25; in it, one can visually see how the pixel's magnitude allows it to stand out strongly in the field of lesser clutter pixels. Also of note is the larger separation between the distributions of the target pixels and the clutter pixels,



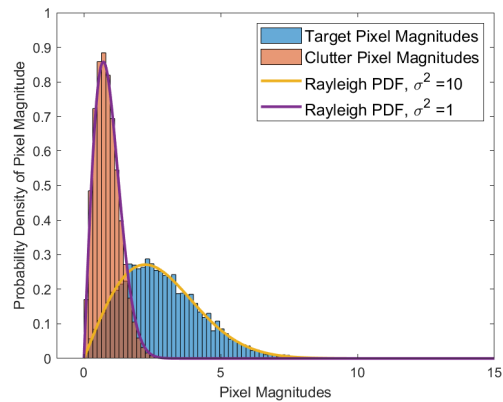
(a) Sample SAR Image, SCR=25



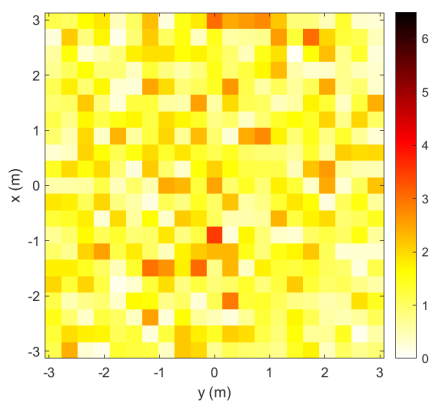
(b) Histograms and Pixel Magnitude Distributions for SCR=25 Images



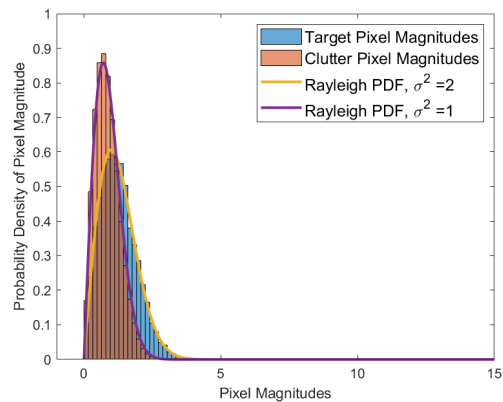
(c) Sample SAR Image, SCR=9



(d) Histograms and Pixel Magnitude Distributions for SCR=9 Images



(e) Sample SAR Image, SCR=1



(f) Histograms and Pixel Magnitude Distributions for SCR=1 Images

Figure 9: Image and Probability Distributions of Target and Clutter Pixel Magnitudes for Images using Different SCRs

which should lend itself to higher target detection performance (as is investigated in greater detail later in this section). Figures 9c and 9d represent the set of SAR images produced using an SCR of 9. The target pixel now possesses a magnitude that is only slightly higher than that of the surrounding clutter pixels; this also is evident from the magnitude distributions, where there is less separation and greater overlap than is present in Figure 9b. Images possessing an SCR of 1 are evaluated in Figures 9e and 9f; in Figure 9e, the target pixel is visually indistinguishable from the clutter pixels, as a large portion of the clutter pixels possess a higher magnitude. From the magnitude distributions in Figure 9f, it should be noted that there is very little separation between the clutter and target distributions, which would make target detection challenging before any type of errors are even considered.

### 4.3 Effects of Motion Measurement Errors

Next, in order to accurately assess the relationship between image quality (measured through IQMs) and target detection, the image quality of all 50000 images is degraded by inserting MMEs into the relevant phase histories before image formation takes place. Four varying levels of error are utilized for each of three different types of MME, as shown in Table 6.

Table 6: Theoretical vs Simulated Clutter Pixel Statistics

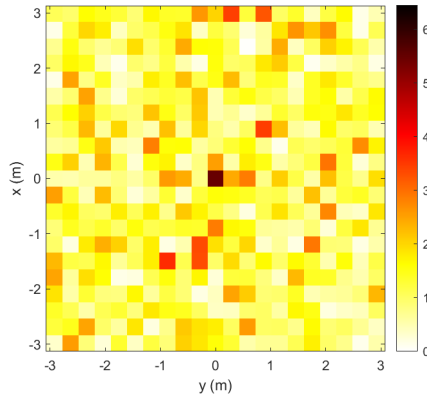
MME Type	Symbol	MME Levels	Units
Position Measurement Error	$p_{err}$	0, 0.1, 0.2, 0.3	m
Velocity Measurement Error	$v_{err}$	0, 0.25, 0.5, 1.0	m/s
Acceleration Measurement Error	$a_{err}$	0, 0.25, 0.5, 0.1	m/s <sup>2</sup>

Figures 10, 11, and 12 show the resultant PDFs for the target and clutter pixel magnitudes after application of the related MME, as compared to their pre-MME pixel magnitudes. The blue histogram bars represent the distribution of target pixel magnitudes before MME application, while red bars represent the target magnitudes

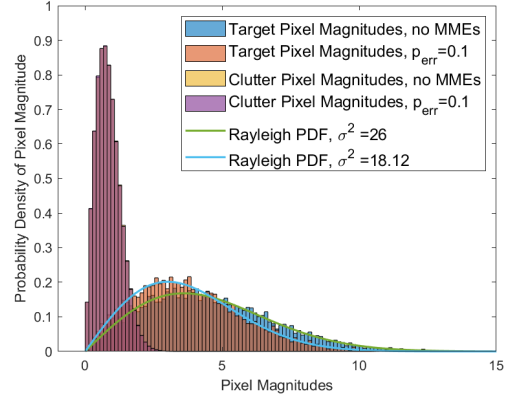
after MME application. Likewise, yellow bars represent clutter distributions pre-MME, and purple bars represent clutter distributions post-MME. The yellow bars are generally not visible because there is such little change between the clutter's pre- and post-MME distributions, so the red bars almost completely overlap the blue ones.

Recall that closed-form equations could not be derived for phase history or image formation after application of MMEs; therefore, the effects of MME insertion must be assessed via measurements and quantitative comparisons. Sample SAR images and histograms are again utilized to assist with this evaluation; the initial focus is on images possessing an SCR of 25, as these images more strongly demonstrate the effects of the MMEs than those of lesser SCRs. Figures 10a, 10c, and 10e contain sample images for the three levels of position measurement error, taken from the 10000 images characterized by an SCR of 25, while Figures 10b, 10d, and 10f depict the pixel magnitude distributions for the same set of 10000 images due to the varying position measurement errors. These figures show that the position error of 0.1 m does not cause a significant change in the target pixel distributions, while the 0.2-m position error cuts the standard deviation of the target pixel magnitude in half, which would equate to reducing the SCR to a quarter of its original value. Finally, a position error of 0.3 m causes the target pixel magnitude's probability density to exactly match that of the clutter pixels, as this error causes the resultant images to depict the target as centered in the pixel *next to* the pixel of its actual location, while reducing the magnitude of the true target pixel to that of a clutter pixel.

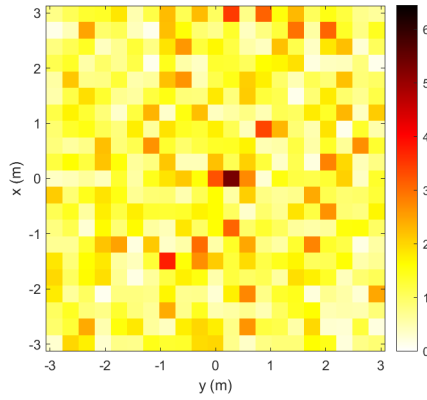
Figures 11a-11f feature the effects of varying velocity measurement errors, again on images with an SCR of 25. As might be expected, the figures show that increasing the velocity error from 0.25 m/s to 0.5 m/s and then 1.0 m/s correspondingly shifts the the target pixel magnitude's probability density further to the left, though not in a linear fashion. This reduction in effective SCR can be attributed to the fact that



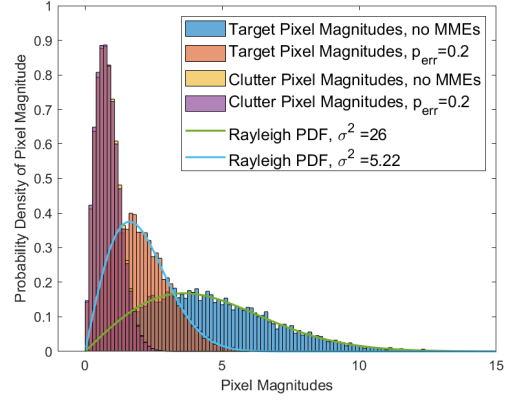
(a) Position measurement error of 0.10 m



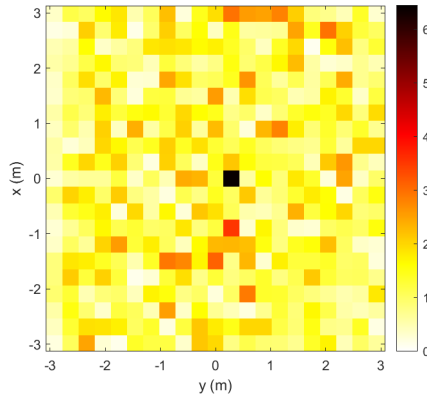
(b) Position measurement error of 0.10 m



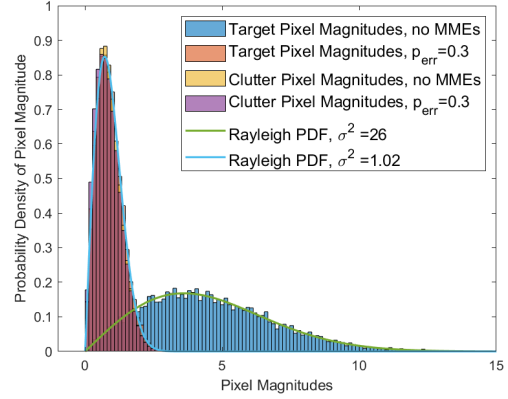
(c) Position measurement error of 0.20 m



(d) Position measurement error of 0.20 m

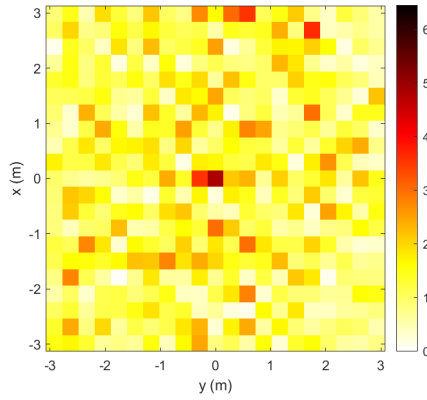


(e) Position measurement error of 0.30 m

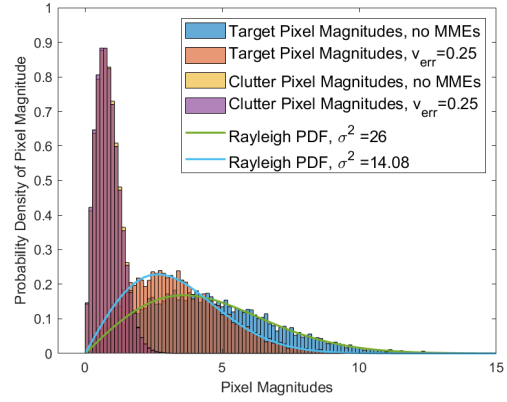


(f) Position measurement error of 0.30 m

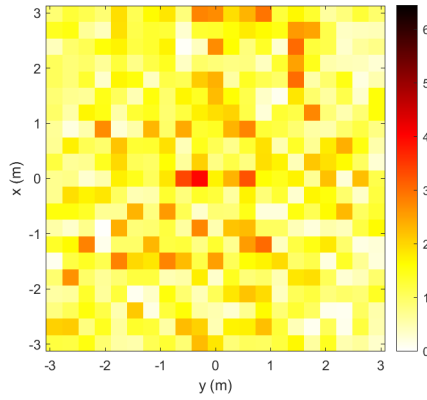
Figure 10: Probability Densities of Target and Clutter Pixel Magnitudes in Images with SCR of 25, after applying varying levels of position measurement error



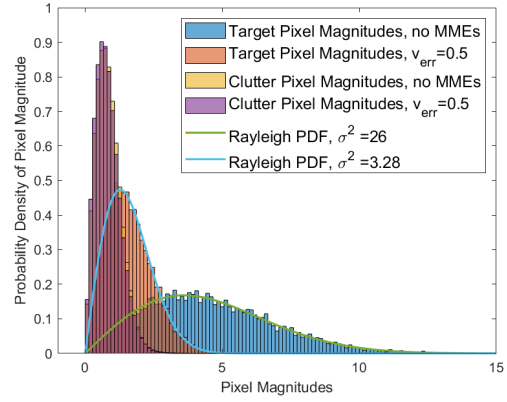
(a) Velocity measurement error of 0.25 m



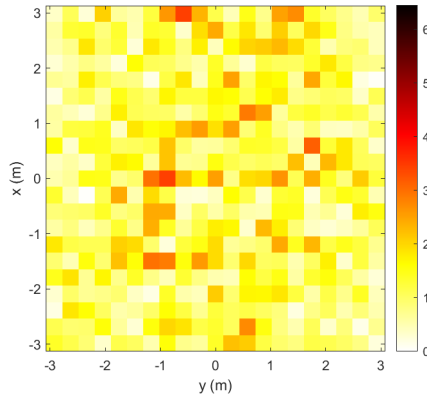
(b) Velocity measurement error of 0.25 m/s



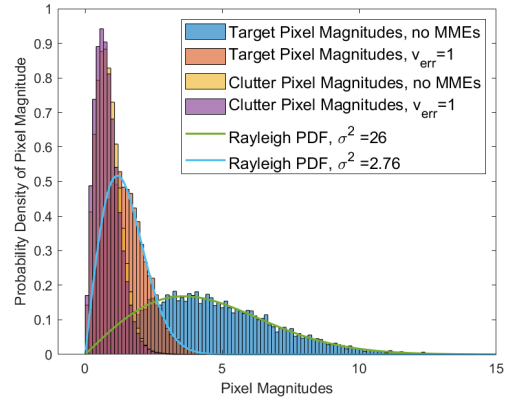
(c) Velocity error of 0.50 m



(d) Velocity error of 0.5 m/s



(e) Velocity error of 1.0 m



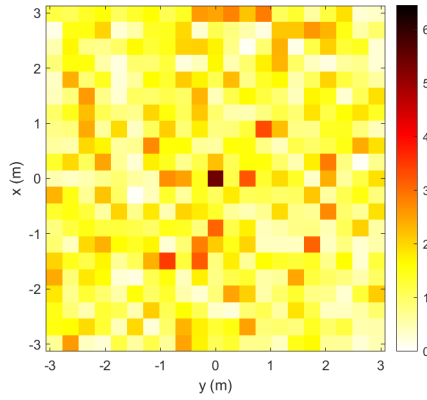
(f) Velocity error of 1.0 m/s

Figure 11: Histograms of Target and Clutter Pixel Magnitudes in Images of SCR = 25, after applying varying levels of velocity measurement error

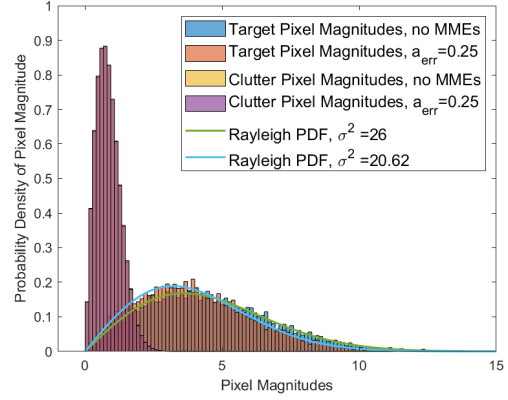
the increasing levels of velocity measurement error causes the signal energy to spread out to neighboring pixels, dissipating the target pixel's magnitude towards that of clutter; however, it must be reiterated that this dissipation does not appear to be linear, so greater errors in velocity measurement do not necessarily result in greater decreases in target pixel magnitude or SCR.

Figures 12a-12f display the effects of the varying acceleration measurement errors on the SCR=25 images. As with the previous two types of measurement errors, increasing levels of acceleration measurement error result in decreasing magnitudes for the target pixel. Examination of Figures 12a, 12c, and 12e allows inference that this magnitude reduction is again a consequence of signal energy dissipation and spread to neighboring pixels, though exploration of acceleration measurement errors earlier in this thesis indicated that the energy spread occurs primarily in one direction; this distinction is difficult to evaluate visually in the related figures. This contrasts with the spread caused by velocity measurement errors, which was clearly seen as affecting neighboring pixels in both along-track directions in Figures 11a, 11c, and 11e. It must also be noted that, in the cases of both velocity and acceleration measurement errors, the signal energy spread exhibited a much less evident effect on the distribution of clutter pixels; this can be attributed to the fact that the clutter pixel amplitudes are already quite similar to each other (i.e., their variance is already quite low). Smearing the energy of a target pixel with amplitude 5 into a neighborhood of clutter pixels that each possess an amplitude of 1 will greatly lower the amplitude of the target pixel and slightly raise the amplitude of the clutter pixels, but smearing the energy of a clutter pixel of amplitude 1 (or 0.9, or 1.1, etc.) that is surrounded by similar clutter pixels will not affect any of those pixels much. Assuredly, the lower the variance is amongst a group of pixels, the less effect the application of an MME will have on them.

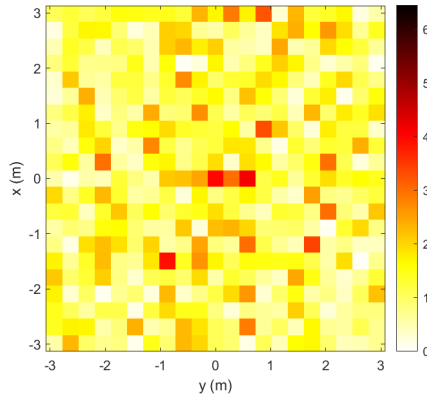




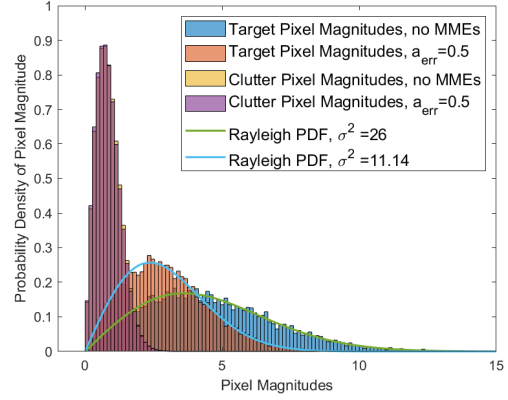
(a) Accel measurement error of 0.25 m/s<sup>2</sup>



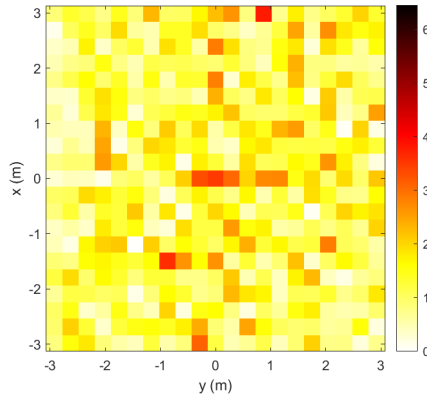
(b) Accel measurement error of 0.25 m/s<sup>2</sup>



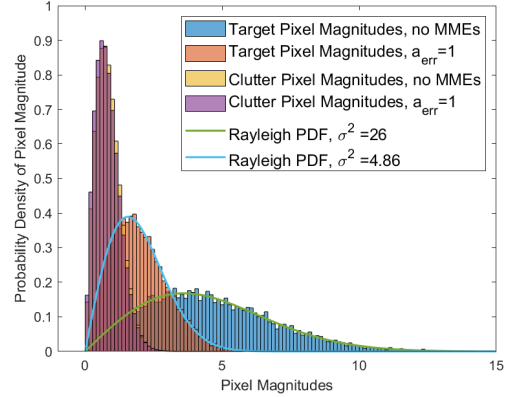
(c) Accel measurement error of 0.50 m/s<sup>2</sup>



(d) Accel measurement error of 0.5 m/s<sup>2</sup>

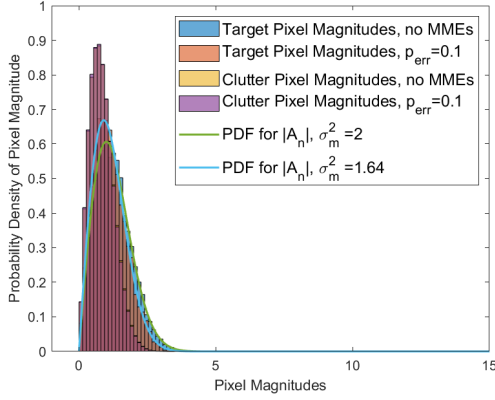


(e) Accel measurement error of 1.0 m/s<sup>2</sup>

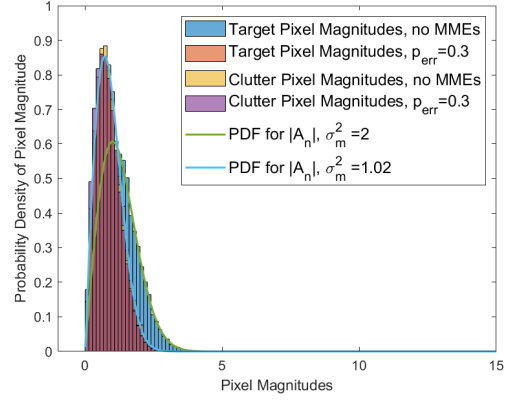


(f) Accel measurement error of 1.0 m/s<sup>2</sup>

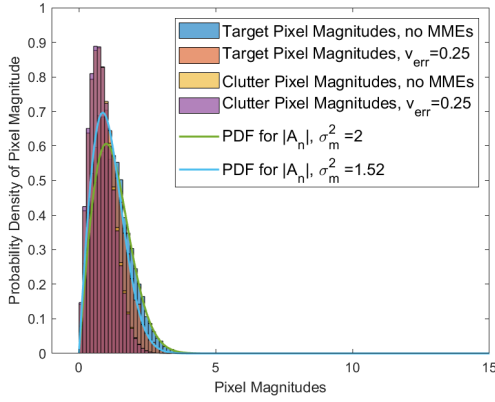
Figure 12: Histograms of Target and Clutter Pixel Magnitudes in Images of SCR = 25, after applying varying levels of acceleration measurement error



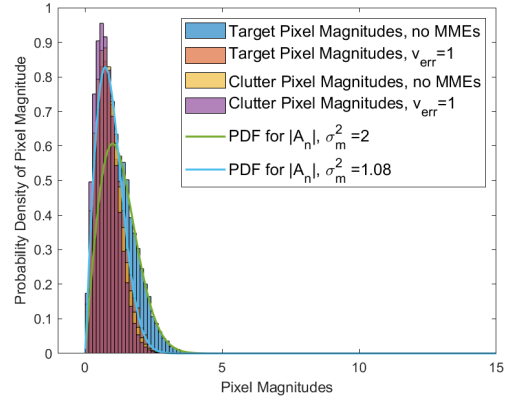
(a) Position error of 0.10 m



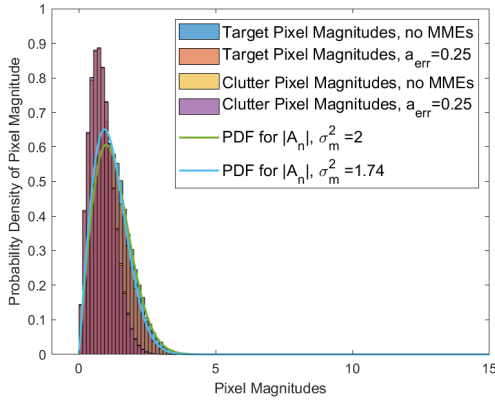
(b) Position error of 0.30 m



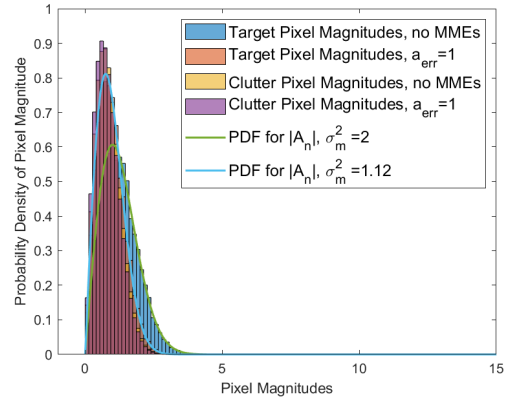
(c) Velocity error of 0.25 m/s



(d) Velocity error of 1.0 m/s



(e) Acceleration error of 0.25 m/s<sup>2</sup>



(f) Acceleration error of 1.0 m/s<sup>2</sup>

Figure 13: Histograms of Target and Clutter Pixel Magnitudes in Images of SCR = 1, after applying varying levels of motion measurement errors

The histograms in Figures 13a-13f depict the pixel magnitude distributions for images composed with an SCR of 1, both before and after the relevant MMEs have been applied. In all cases, the target pixel's magnitude distribution after MME application is virtually indistinguishable from that of clutter. This can be directly attributed to the fact that the target pixel magnitude distribution closely resembles that of clutter pixels, pre-MME application. However, it should be noted that for every type of MME, the post-MME target pixel magnitude distribution draws even closer to that of clutter, causing effective SCR to approach nearer to 1. It can be expected that target detection proves to be difficult using images with an SCR of 1, regardless of the presence of MMEs; this task would become virtually impossible to perform with any true success after introducing MMEs to SAR images in which the signal and clutter levels are already equal.

#### 4.4 Target Detection Performance

To perform analysis of target detection performance, all five sets of 10000 unadulterated SAR images are first run through the CFAR detector described in Section 3.5 to set a performance baseline for each SCR scenario, unaffected by MMEs. For each detection trial, the CFAR stencil shown in Figure 8 is set over each pixel to individually test them using the test statistic as described in Section 3.5. The computed test statistic is then compared to a specific threshold predetermined in accordance with the desired false alarm rate. True detections and false alarms are recorded as the detector runs through each pixel in each of the 10000 images in the SCR set; then the threshold level is raised slightly, and all 10000 trials are run again. At least twenty threshold levels are tested per Monte Carlo run. After establishment of this performance baseline, the same target detection trials are next run under each MME condition, such that each full set of 50000 images (all five SCR groups) are tested

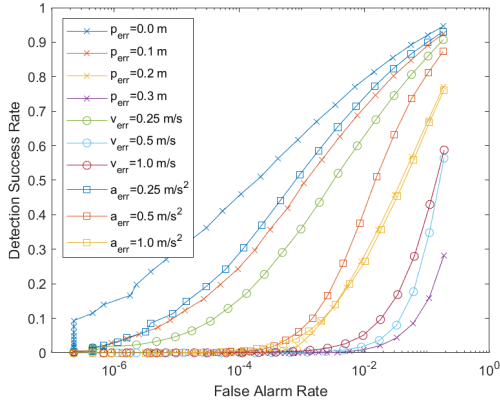
nine additional times (once for each unique level of the three MME types). Data from the baseline trials and the nine MME-affected trials are aggregated into ROC curves to visually demonstrate the effects of each MME on the PD against constant rates of false alarm; these ROC curves are displayed as Figures 14a-14e.

From the ROC curves displayed in Figures 14a-14e, it is evident that the probability of target detection decreased for each decrease in image SCR. Especially noteworthy is the fact that, once a respectable false alarm rate is set for images of SCR=1 (i.e.,  $P_{FA} < 10^{-2}$ ), the PD does not exceed 10%, even without the presence of MMEs; this falls in line with previous observations of this class of images. Also notable is that, when there is 0.30 meters of position measurement error present, the maximum achievable PD *for the omnisciently-known true target location* is less than 30% regardless of image SCR, meaning that such erroneous measurements reduce the chances of accurate target detection by more than one-third. Note that, if target location did not matter, than the 0.3-m position measurement error would have absolutely no affect on PD.

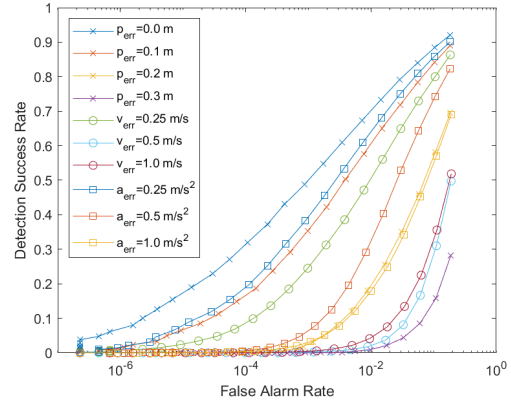
Table 7: Highest PDs Achieved for each SCR/MME Combination

MME	SCR=25	SCR=16	SCR=9	SCR=4	SCR=1
No MME	0.9457	0.9206	0.8750	0.7636	0.5190
$p_{err} = 0.10$ m	0.9237	0.8897	0.8300	0.7017	0.4631
$p_{err} = 0.20$ m	0.7697	0.6948	0.5940	0.4622	0.3328
$p_{err} = 0.30$ m	0.2820	0.2827	0.2834	0.2835	0.2838
$v_{err} = 0.25$ m/s	0.9073	0.8633	0.7909	0.6523	0.4258
$v_{err} = 0.50$ m/s	0.5638	0.4976	0.4304	0.3633	0.3067
$v_{err} = 1.00$ m/s	0.5876	0.5186	0.4389	0.3572	0.3000
$a_{err} = 0.25$ m/s <sup>2</sup>	0.9303	0.9009	0.8492	0.7312	0.4838
$a_{err} = 0.50$ m/s <sup>2</sup>	0.8731	0.8233	0.7407	0.5976	0.3996
$a_{err} = 1.00$ m/s <sup>2</sup>	0.7610	0.6897	0.5884	0.4584	0.3420

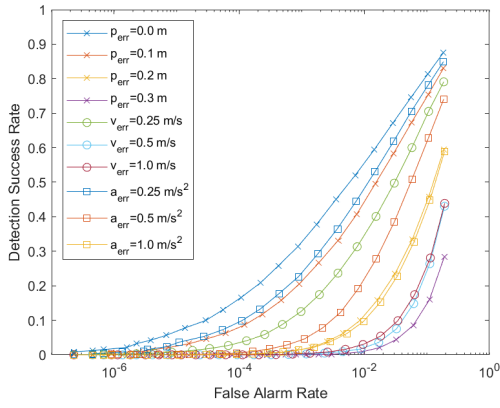
To maximize visualization of these trends, the highest PDs achieved by each distinct MME for each SCR set is isolated and then combined them into a single plot, as shown in Figure 15. This figure displays the downward non-linear trend in proba-



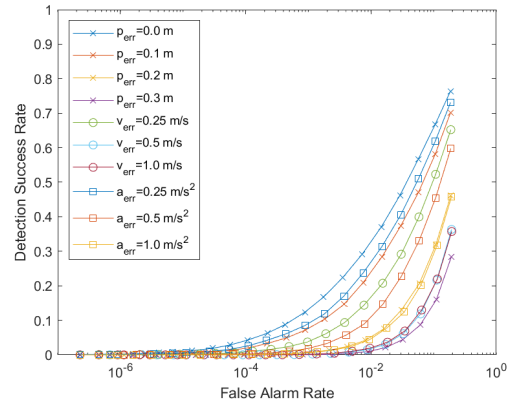
(a) ROC Curves for SCR=25



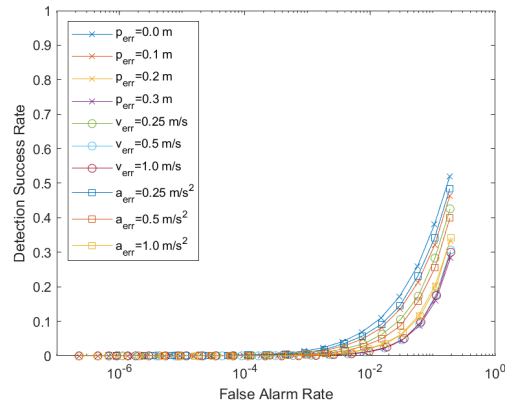
(b) ROC Curves for SCR=16



(c) ROC Curves for SCR=9



(d) ROC Curves for SCR=4



(e) ROC Curves for SCR=1

Figure 14: ROC Curves with varying levels of motion measurement errors applied, for each SCR

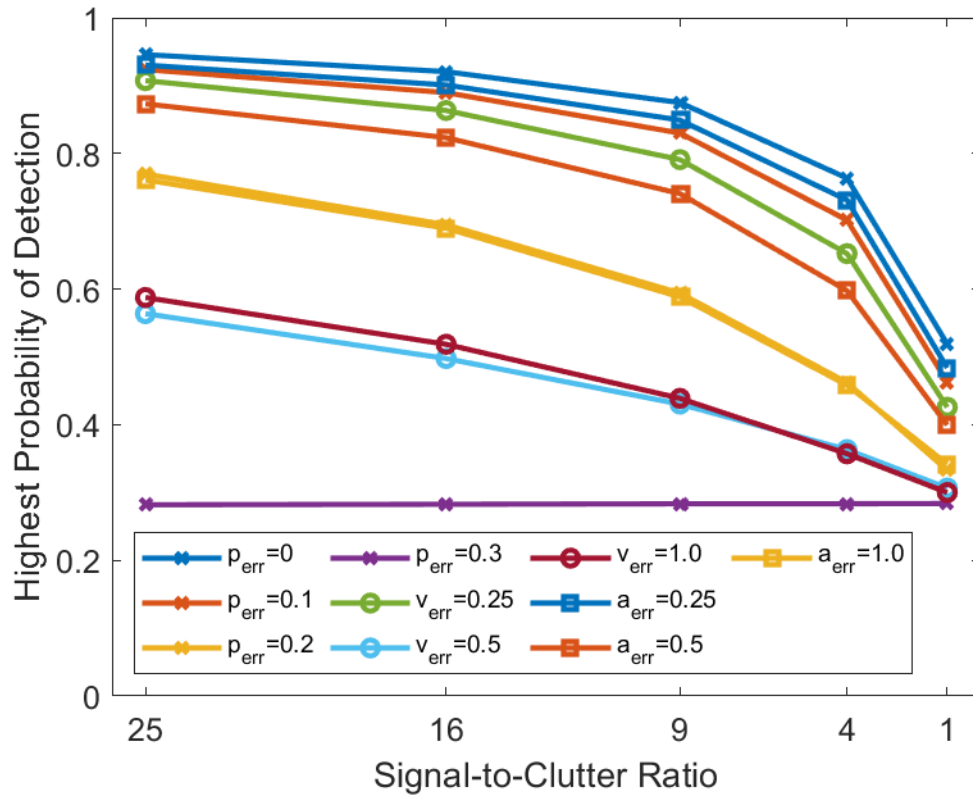


Figure 15: Highest Simulated Probability of Detection for each MME applied, at each SCR

bility of detection for all images as SCR decreases, regardless of MME levels. Figure 15 also depicts how the applied amount of MME affects probability of detection; for example, the detector can achieve a PD of 87.5% on images with an SCR of 9 and no MMEs, but PD drops below 60% when a position measurement error of 0.2 m is applied, 50% when  $v_{err} = 0.5$  m/s, and below 30% when  $p_{err} = 0.3$  m. Further data for Figure 15 can be found in Table 7.

In general, Figure 15 indicates that the applied MMEs affected probability of detection disproportionately, in the following order from least to greatest effect:

1. Acceleration Measurement Error of 0.25 m/s<sup>2</sup>
2. Position Measurement Error of 0.10 m
3. Velocity Measurement Error of 0.25 m/s
4. Acceleration Measurement Error of 0.50 m/s<sup>2</sup>
5. Position Measurement Error of 0.20 m
6. Acceleration Measurement Error of 1.0 m/s<sup>2</sup>
7. Velocity Measurement Error of 1.0 m/s
8. Velocity Measurement Error of 0.50 m/s
9. Position Measurement Error of 0.30 m

Due to the strong relation between the type and amount of MME and its effect on probability of detection, all further data in this thesis will be listed in this order. There are a few exceptions to this order evident in Table 7 and Figure 15; specifically, a higher PD is achieved when  $v_{err} = 0.5$  m/s than when  $v_{err} = 1.0$  m/s for images with SCRs of 4 and 1, and a higher PD is also achieved when  $a_{err} = 1.0$  m/s<sup>2</sup> or when  $v_{err} = 0.5$  m/s, for SCR=1 images only. In addition, there is essentially a flat line for the highest PDs produced after application of 0.3 m of position measurement error, meaning SCR strength does not affect detection outcomes in light of such erroneous measurements because the detector falsely detects the target in a

neighboring pixel, regardless of SCR. However, these small deviations do not detract from the general observed trend. Of particular note is that, for images with strong SCRs, velocity measurement errors of 0.50 m/s caused lower detection probabilities than the greater velocity measurement error of 1.0 m/s. This observance is the only one that violates the expected relation that greater MMEs result in lower detection probabilities; previous observations regarding signal energy spread from velocity measurement errors do not fully explain this result. More research into this phenomena should be considered.

#### 4.5 IQM Analysis

Now that the amount of MME has been sufficiently linked to probability of detection, the impact MMEs have on IQMs can be examined, as well as the linkage between IQMs and PD. For this thesis, five IQMs were selected: two contrast metrics, one sharpness metric, and two entropy metrics. In order to produce comparable data between all IQMs (or as the aphorism goes, “to compare apples to apples”), first the respective IQMs are calculated for every single image, both with and without the 9 MMEs, for the entire Monte Carlo set of 10000 images at each of the 5 SCRs, covering every possible MME-SCR image combination produced thus far. Then the mean and standard deviation of each IQMs is then calculated for each MME-SCR combination, and those means and standard deviations are finally normalized by dividing by the mean IQMs of the “No MME + SCR=25” group, as that group has proven to allow the highest PD in all instances. For this reason, you will see that the “No MME + SCR=25” metric value for each IQM is equal to 1. Each IQM is examined separately below.



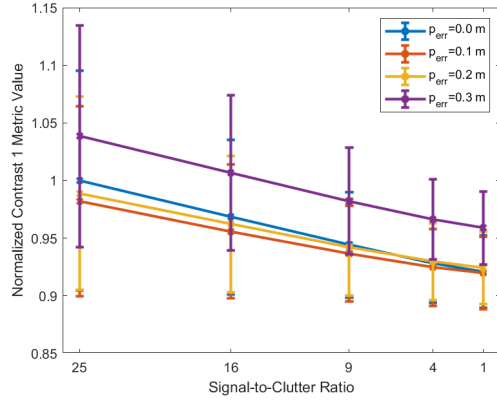
#### 4.5.1 Contrast

Table 8 represents the normalized mean Contrast 1 metric data calculated for all MME-SCR combinations, listed in order of MMEs that have the least to greatest effect on PD. Figures 16a-16c separate Table 8's data into the three separate MME types: position, velocity, and acceleration. Contrast 2 metric data is depicted in the same manner, with Table 9 containing the tabular data and Figures 17a-17c presenting the data in the separate MME plots.

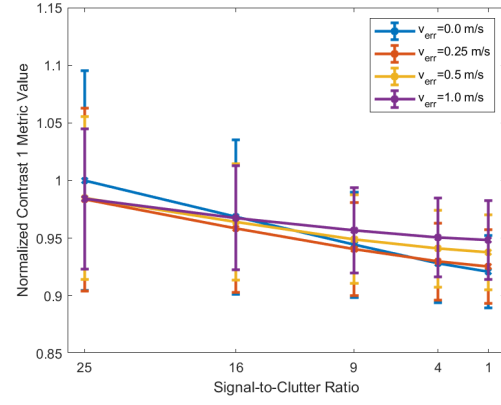
Table 8: Normalized Mean Contrast 1 Values at each MME and SCR level

MME	SCR=25	SCR=16	SCR=9	SCR=4	SCR=1
No MME	1.000	0.9689	0.9451	0.9294	0.9222
$a_{err} = 0.25 \text{ m/s}^2$	0.9845	0.9581	0.9384	0.9258	0.9204
$p_{err} = 0.10 \text{ m}$	0.9887	0.9623	0.9426	0.9302	0.9249
$v_{err} = 0.25 \text{ m/s}$	0.9835	0.9591	0.9413	0.9306	0.9263
$a_{err} = 0.50 \text{ m/s}^2$	0.9831	0.9582	0.9400	0.9292	0.9249
$p_{err} = 0.20 \text{ m}$	0.9822	0.9565	0.9375	0.9257	0.9208
$a_{err} = 1.00 \text{ m/s}^2$	0.9967	0.9737	0.9570	0.9471	0.9430
$v_{err} = 1.00 \text{ m/s}$	0.9847	0.9684	0.9576	0.9518	0.9495
$v_{err} = 0.50 \text{ m/s}$	0.9845	0.9639	0.9495	0.9414	0.9382
$p_{err} = 0.30 \text{ m}$	1.039	1.007	0.9832	0.9674	0.9602

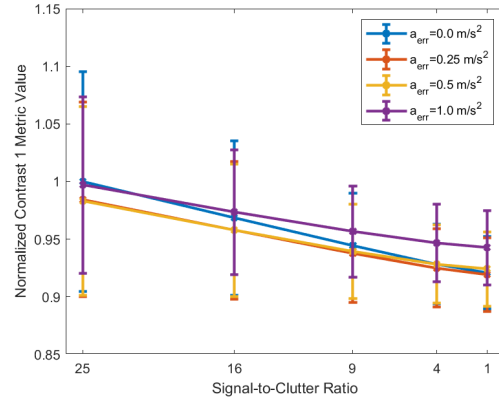
A cursory examination of the Table 8 data does not demonstrate a strong connection between the metric values and the achieved probability of detection levels. Since the normalized mean “No MME, SCR=25” value is (supposed to be) higher than metric values for all other MME-SCR combinations, it would be a fair assumption that lower quantities of MMEs and higher SCRs would equate to higher Contrast 1 values, which would then translate to higher detection levels. While the trend of higher SCR values producing higher contrast values holds true throughout, the MME quantities do not seem to hold the same type of relationship with Contrast 1 metrics. A close look at each SCR column shows that all related MME quantities possess normalized mean Contrast 1 values that are within 0.2 units of each other, which



(a) Contrast 1 Metrics for Position Measure-



(b) Contrast 1 Metrics for Velocity Measure-



(c) Contrast 1 Metrics for Acceleration Mea-

Figure 16: Contrast 1 Metrics for each MME at each SCR

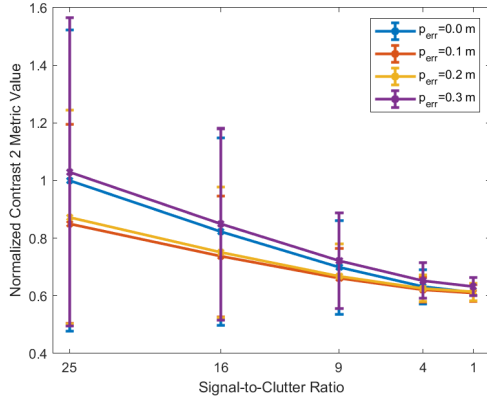
means they would all fall within a tolerance of  $\pm 0.1$ . The single odd exception is that of the 0.30-m position measurement error, which continuously possessed the highest contrast values for each SCR...even higher than that of the error-less mean contrast values.

These observations are further backed up by the plots in Figures 16a-16c. Figure 16a shows that the “ $p_{err} = 0.30$  m” error produces higher contrast values than the other position errors, while Figures 16b and 16c demonstrate how there is no truly tangible trend other than that of diminishing contrast values as SCR is decreased.

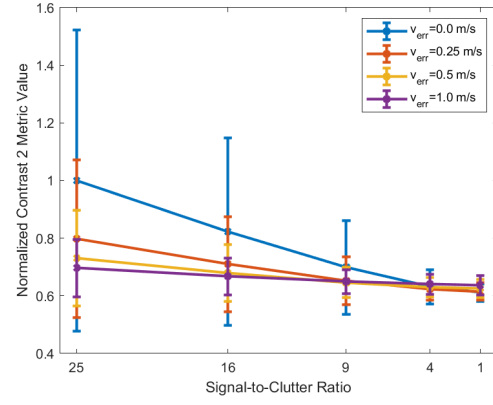
Table 9: Normalized Mean Contrast 2 Values at each MME and SCR level

MME	SCR=25	SCR=16	SCR=9	SCR=4	SCR=1
$p_{err} = v_{err} = a_{err} = 0$	1.000	0.823	0.709	0.643	0.623
$a_{err} = 0.25$ m/s <sup>2</sup>	0.894	0.761	0.680	0.634	0.621
$p_{err} = 0.10$ m	0.852	0.740	0.671	0.632	0.620
$v_{err} = 0.25$ m/s	0.803	0.717	0.664	0.634	0.626
$a_{err} = 0.50$ m/s <sup>2</sup>	0.794	0.709	0.659	0.632	0.625
$p_{err} = 0.20$ m	0.879	0.754	0.678	0.637	0.624
$a_{err} = 1.00$ m/s <sup>2</sup>	0.808	0.721	0.671	0.645	0.637
$v_{err} = 1.00$ m/s	0.706	0.677	0.661	0.652	0.650
$v_{err} = 0.50$ m/s	0.738	0.687	0.657	0.641	0.637
$p_{err} = 0.30$ m	1.016	0.849	0.732	0.665	0.643

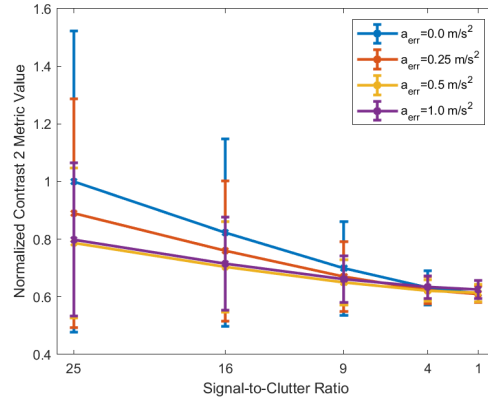
Table 9 data for Contrast 2 and Figures 17b-17c demonstrate a subtly stronger relationship between the IQM, MMEs, and relative detection performance than was apparent for Contrast 1. For example, higher Contrast 2 metric values are more clearly aligned with certain MME levels for SCRs of 25, 16, and 9, although the MMEs linked to higher contract values are not necessarily the ones linked to better (or worse) detection performance. Figure 17a appears to demonstrate that the Contrast 2 values for the error-free and 0.3-m position error images were statistically equal to each other for all SCRs, while the contrast values for the 0.1- and 0.2-m position error images were also statistically equivalent over all SCRs. The values for Contrast 2 certainly demonstrate stronger trends than those for Contrast 1.



(a) Contrast 2 Metrics for Position Measure-



(b) Contrast 2 Metrics for Velocity Measurement Errors



(c) Contrast 2 Metrics for Acceleration Measurement Errors

Figure 17: Contrast 2 Metrics for each MME at each SCR

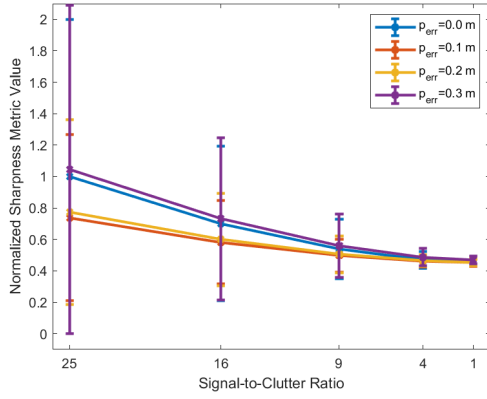
### 4.5.2 Sharpness

Table 10 and Figures 18a-18c provide visual presentation for the sharpness metric, and follow the same format used in the tables and figures for contrast.

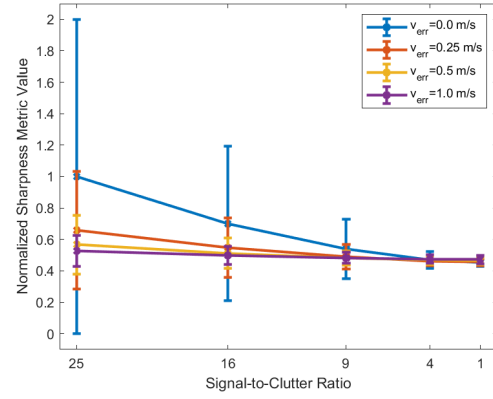
Table 10: Normalized Mean Sharpness Values at each MME and SCR level

MME	SCR=25	SCR=16	SCR=9	SCR=4	SCR=1
$p_{err} = v_{err} = a_{err} = 0$	1.000	0.708	0.557	0.487	0.470
$a_{err} = 0.25 \text{ m/s}^2$	0.817	0.620	0.524	0.480	0.469
$p_{err} = 0.10 \text{ m}$	0.744	0.593	0.515	0.478	0.469
$v_{err} = 0.25 \text{ m/s}$	0.669	0.563	0.506	0.479	0.473
$a_{err} = 0.50 \text{ m/s}^2$	0.658	0.554	0.502	0.478	0.472
$p_{err} = 0.20 \text{ m}$	0.789	0.610	0.521	0.482	0.472
$a_{err} = 1.00 \text{ m/s}^2$	0.673	0.564	0.512	0.488	0.481
$v_{err} = 1.00 \text{ m/s}$	0.544	0.515	0.501	0.493	0.491
$v_{err} = 0.50 \text{ m/s}$	0.581	0.527	0.499	0.485	0.481
$p_{err} = 0.30 \text{ m}$	1.025	0.738	0.578	0.505	0.486

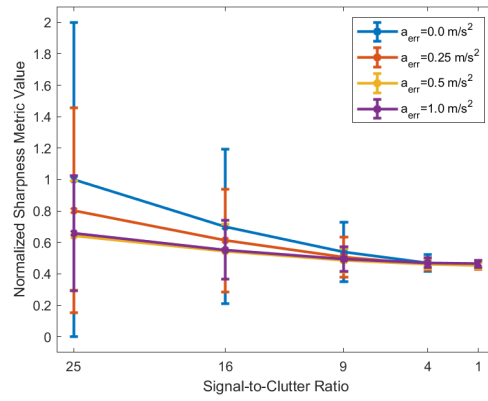
The Sharpness metric seems to be quite similar to that of Contrast 2 and follows the same general trend of diminishing sharpness aligning with decreasing MME-related detection performance levels, except for the position measurement errors. The most noticeable difference between the normalized mean Contrast 2 and Sharpness metrics is that the standard deviation for Sharpness values is much greater, stretching the possible range of Sharpness values from 0.0 to 2.0, as opposed to 0.5 to 1.5 for Contrast 2 values. The greater standard deviation would make the Sharpness metric somewhat less reliable than the Contrast 2 metric. This is unfortunate, as there is an appreciable drop in sharpness as the amount of applied MME increases; for example, images with an SCR of 25 and a velocity measurement error of 1.00 m/s achieve approximately 54% of the sharpness of images with the same SCR but with no MMEs. This phenomena would theoretically work well to help predict target detection success, except that it only holds true for images with high SCRs (25 and 16), and does not follow the same trend for position errors. The latter exception should



(a) Sharpness Metrics for Position Measure-



(b) Sharpness Metrics for Velocity Measurement Errors



(c) Sharpness Metrics for Acceleration Measurement Errors

Figure 18: Sharpness Metrics for each MME at each SCR

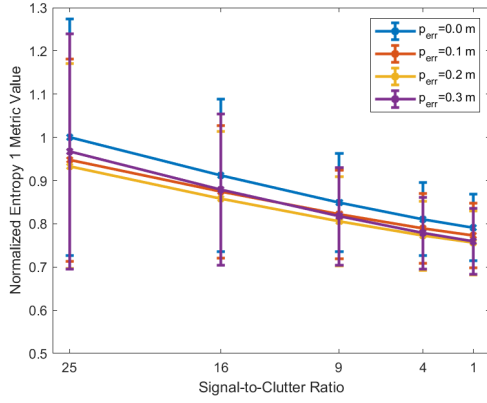
be expected, as the position of a target within a pixel should have no true affect on image sharpness.

### 4.5.3 Entropy

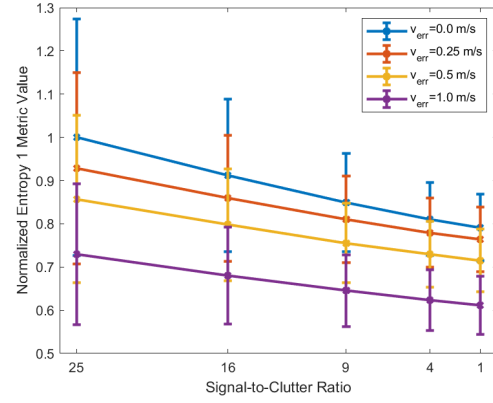
MME	SCR=25	SCR=16	SCR=9	SCR=4	SCR=1
$p_{err} = v_{err} = a_{err} = 0$	1.000	0.915	0.855	0.816	0.799
$a_{err} = 0.25 \text{ m/s}^2$	0.953	0.879	0.827	0.793	0.778
$p_{err} = 0.10 \text{ m}$	0.948	0.877	0.828	0.795	0.775
$v_{err} = 0.25 \text{ m/s}$	0.929	0.864	0.816	0.785	0.766
$a_{err} = 0.50 \text{ m/s}^2$	0.925	0.857	0.810	0.779	0.766
$p_{err} = 0.20 \text{ m}$	0.936	0.862	0.811	0.778	0.758
$a_{err} = 1.00 \text{ m/s}^2$	0.863	0.799	0.755	0.726	0.712
$v_{err} = 1.00 \text{ m/s}$	0.731	0.684	0.651	0.628	0.617
$v_{err} = 0.50 \text{ m/s}$	0.859	0.802	0.762	0.735	0.722
$p_{err} = 0.30 \text{ m}$	0.961	0.882	0.823	0.784	0.761

Table 11: Normalized Mean Entropy 1 Values at each MME and SCR level

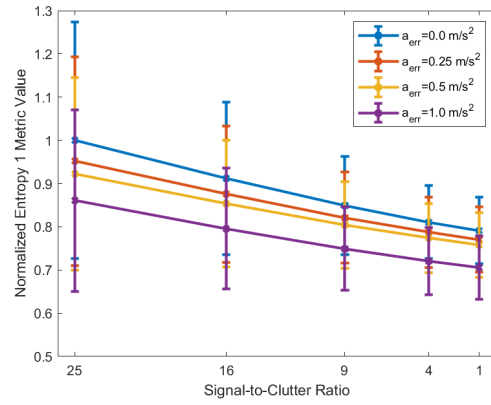
Table 11 indicates that Entropy 1 is the first image quality metric investigated in this thesis for which applying the highest amount of position measurement error does *not* produce a higher metric value than does applying no MME at all. Figures 19b and 19c, demonstrate a very strong relationship between the applied MMEs and the Entropy 1 metric, where higher levels of the former produce lower values of the latter; though this trend does not follow the previously established relationship between MMEs and PD, it does make the most sense intuitively, i.e.  $v_{err} = 1.0 \text{ m/s}$  should (and does) lead to higher entropy than  $v_{err} = 0.50 \text{ m/s}$ . Entropy 1 is also the only metric that possesses statistically differentiated values amongst MMEs of the same class, as the extent of deviation for the average metric value achieved with 1.0 m/s of velocity error does not overlap the deviation achieved before the application of MMEs. This is only true for velocity measurement errors on images with an SCR of 9 and below, but it can be inferred that even higher levels of MME would produce better differentiation for higher SCRs. Figure 19a indicates that position



(a) Entropy 1 Metrics for Position Measure-



(b) Entropy 1 Metrics for Velocity Measurement Errors



(c) Entropy 1 Metrics for Acceleration Measurement Errors

Figure 19: Entropy 1 Metrics for each MME at each SCR

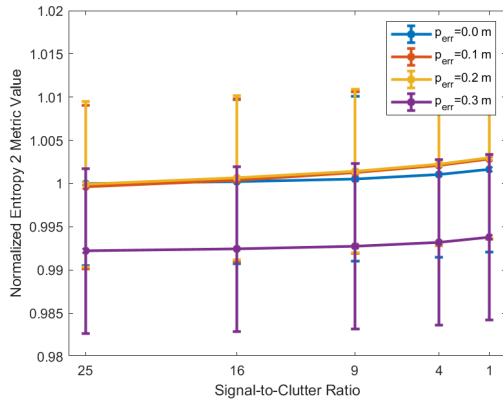


measurement errors fail to produce the same type of trend that is evident with the other two MME types.

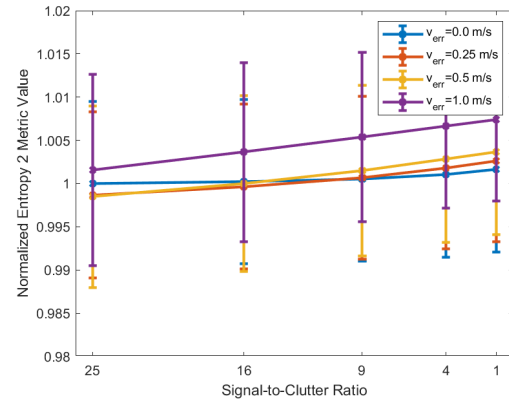
MME	SCR=25	SCR=16	SCR=9	SCR=4	SCR=1
$p_{err} = v_{err} = a_{err} = 0$	1.000	1.000	1.000	1.001	1.002
$a_{err} = 0.25 \text{ m/s}^2$	1.000	1.001	1.001	1.002	1.003
$p_{err} = 0.10 \text{ m}$	1.000	1.000	1.001	1.002	1.003
$v_{err} = 0.25 \text{ m/s}$	0.999	1.000	1.001	1.002	1.003
$a_{err} = 0.50 \text{ m/s}^2$	0.999	1.000	1.001	1.002	1.003
$p_{err} = 0.20 \text{ m}$	1.000	1.001	1.002	1.003	1.003
$a_{err} = 1.00 \text{ m/s}^2$	0.998	0.999	1.000	1.002	1.002
$v_{err} = 1.00 \text{ m/s}$	1.002	1.004	1.005	1.007	1.007
$v_{err} = 0.50 \text{ m/s}$	0.998	1.000	1.001	1.003	1.004
$p_{err} = 0.30 \text{ m}$	0.992	0.992	0.992	0.993	0.994

Table 12: Normalized Mean Entropy 2 Values at each MME and SCR level

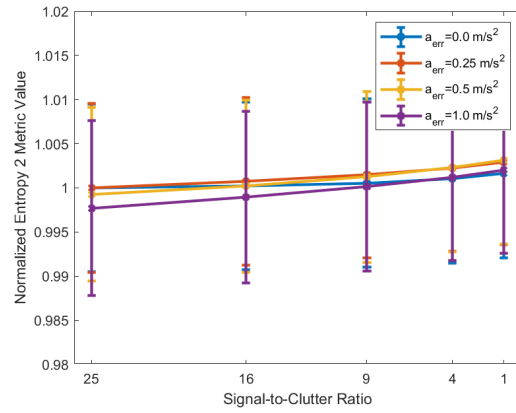
No connections or trends can, nor should, be taken from the data in Table 12 for Entropy 2 because the values are all so close together, they could be considered one and the same. The two minor exceptions are the metric values for  $v_{err} = 1.00 \text{ m/s}$  and  $p_{err} = 0.30 \text{ m}$ , but even their values are separated from that of no MMEs by only 0.8%. Figures 20a - 20c further emphasize the point that Entropy 2 does not provide any useful trends, other than a statistically-insignificant increase in metric value as the SCR decreases.



(a) Entropy 2 Metrics for Position Measure-  
ment Errors



(b) Entropy 2 Metrics for Velocity Measure-  
ment Errors



(c) Entropy 2 Metrics for Acceleration Mea-  
surement Errors

Figure 20: Entropy 2 Metrics for each MME at each SCR

## V. Conclusions

### 5.1 Key Conclusions

The results of Chapter IV indicate that there are a variety of factors to consider when attempting to increase a SAR system's probability of detection through improved image quality. They are as follows:

- It is clear that the signal-to-clutter ratio utilized in acquiring the phase history data that is necessary to form the SAR image has a direct and demonstrable effect on the system's ability to detect point targets.
- Motion measurement errors also have a demonstrable effect on target detection success, as our simulation testing has shown that larger amounts of MMEs lead to lower probabilities of detection. However, the connection between MMEs and detection probability is less clear once SCR falls to 4 or lower; this discrepancy indicates that a minimum SNR floor above 4 should be strongly considered for target detection improvements.
- Our results indicate that higher levels of signal-to-clutter ratios improve image quality metrics, except in the case of one particular type of entropy metrics. This relationship was most demonstrable for sharpness metrics, but was also apparent for contrast and entropy 1 metrics as well.
- The only conclusion we could draw with at least a medium level of confidence regarding the relationship between image quality metrics and motion measurement errors is that one certain type of entropy metrics works well for indicating the presence of velocity measurement errors in images formed with low SCRs (SCR=9 and below). Results seem to indicate that this scope could widen to acceleration measurement errors and images with higher SCRs; further investigation into this region should be performed with a wider range of MMEs and

SCRs.

- We were unable to draw a strong connection between the image quality metrics investigated in this thesis, and probability of detection. This incapacity was further perpetuated by the unpredictable effect of position measurement errors on contrast and sharpness metrics.

## 5.2 Significance of the Research

Using the detection algorithm described in Chapter III, we were able to characterize the effects of varying signal-to-clutter ratios on a SAR system's target detection performance. We were also able to characterize the effects of applying various levels of position, velocity, and acceleration measurement errors on the probability of target detection. We investigated the relationships, or lack thereof, between selected image quality metrics, signal-to-clutter ratios, motion measurement errors, and the probability of target detection. The results of this thesis will better inform radar engineers on signal formation and image processing criteria that are more likely to result in heightened target detection success. This thesis should also provide some insight into the image quality metrics that can best indicate the presence of motion measurement errors, allowing radar engineers to focus their time and energy on researching and producing autofocus algorithms based on the best subset of IQMs.

## 5.3 Future Work

The results of this work could be extended by:

- Utilizing an incoherent detector, as opposed to the coherent detector used in this thesis, to ensure that results remain the same regardless of detector type
- Increasing the number of signal-to-clutter ratios tested within the established range, to solidify the results encountered within this thesis and encounter the

specific breaking point for the relationship between SCRs and MMEs.

- Increasing the range of motion measurement errors simulated and tested, to further investigate any potential relationships between MMEs and target detection.
- Increasing the numbers of MME combinations utilized.
- Widening the scope of image quality metrics utilized in order to discover other IQMs that may be even more beneficial in predicting future target detection success.
- Relating MMEs to radar design parameters; for example, how does position measurement error relate to range and cross-range resolution? How do velocity measurement errors relate to pulse repetition frequency (PRF)? Do acceleration measurement errors relate to scene extent (making quadratic phase errors more noticeable)?
- Testing against tasks other than target detection, such as RCS pattern recovery.

## Bibliography

1. M. A. Richards, J. A. Scheer, and W. A. Holm, *Principles of Modern Radar: Basic Principles*. Raleigh, NC: SciTech Publishing, Inc., 2010.
2. M. Skolnik, *Radar Handbook, Third Edition*. Electronics electrical engineering, New York, NY: McGraw-Hill Education, 2008.
3. J. Harris, R. Ostler, D. Chabries, and R. Christiansen, “Quality measures for SAR images,” in *ICASSP-88., International Conference on Acoustics, Speech, and Signal Processing*, vol. 2, pp. 1064–1067, 1988.
4. L. Dell’Amore, M. Villano, G. Krieger, and A. Moreira, “Waveform-encoded synthetic aperture radar: Image quality assessment using satellite data,” in *2019 Kleinheubach Conference*, pp. 1–4, 2019.
5. M. Vespe and H. Greidanus, “SAR image quality assessment and indicators for vessel and oil spill detection,” *IEEE Transactions on Geoscience and Remote Sensing*, vol. 50, no. 11, pp. 4726–4734, 2012.
6. C. Oliver and S. Quegan, *Understanding Synthetic Aperture Radar Images*. Artech House Remote Sensing Library, Artech House, 1998.
7. C. V. Jakowatz, D. E. Wahl, and P. H. Eichel, *Spotlight-Mode Synthetic Aperture Radar: A Signal Processing Approach*. Boston, MA: Boston, MA: Kluwer, May 1996.
8. W. G. Carrara, R. S. Goodman, and R. M. Majewski, *Spotlight Synthetic Aperture Radar: Signal Processing Algorithms*. Norwood, MA: Artech House, 1995.
9. N. J. Willis and H. D. Griffiths, *Advances in Bistatic Radar*. Radar, Sonar, & Navigation, Raleigh, NC: SciTech Publishing, Inc., 2007.

10. D. Munson, J. O'Brien, and W. Jenkins, "A tomographic formulation of spotlight-mode synthetic aperture radar," *Proceedings of the IEEE*, vol. 71, no. 8, pp. 917–925, 1983.
11. M. T. Eugene Knott, John Shaeffer, *Radar Cross Section, 2nd ed.* Artech House, Inc., 1993.
12. A. Freeman, "SAR calibration: an overview," *IEEE Transactions on Geoscience and Remote Sensing*, vol. 30, no. 6, pp. 1107–1121, 1992.
13. B. J. Döring and M. Schwerdt, "The radiometric measurement quantity for SAR images," *IEEE Transactions on Geoscience and Remote Sensing*, vol. 51, no. 12, pp. 5307–5314, 2013.
14. L. A. Gorham and L. J. Moore, "SAR image formation toolbox for MATLAB," in *Algorithms for Synthetic Aperture Radar Imagery XVII* (E. G. Zelnio and F. D. Garber, eds.), vol. 7699, pp. 46 – 58, International Society for Optics and Photonics, SPIE, 2010.
15. B. Rigling and R. Moses, "Polar format algorithm for bistatic SAR," *IEEE Transactions on Aerospace and Electronic Systems*, vol. 40, no. 4, pp. 1147–1159, 2004.
16. R. L. Morrison, M. N. Do, and D. C. Munson, "SAR Image Autofocus By Sharpness Optimization: A Theoretical Study," *IEEE Transactions on Image Processing*, vol. 16, no. 9, pp. 2309–2321, 2007.
17. T. J. Schulz, "Optimal Sharpness Function for SAR Autofocus," *IEEE Signal Processing Letters*, vol. 14, no. 1, pp. 27–30, 2007.
18. Li Xi, Liu Guosui, and Jinlin Ni, "Autofocusing of ISAR images based on entropy minimization," *IEEE Transactions on Aerospace and Electronic Systems*, vol. 35, no. 4, pp. 1240–1252, 1999.

19. J. R. Fienup and J. J. Miller, "Aberration correction by maximizing generalized sharpness metrics," *J. Opt. Soc. Am. A*, vol. 20, pp. 609–620, Apr 2003.
20. Y. Gao, W. Yu, Y. Liu, and R. Wang, "Autofocus algorithm for SAR imagery based on sharpness optimisation," *Electronics Letters*, vol. 50, no. 11, pp. 830–832, 2014.
21. J. N. Ash, "An Autofocus Method for Backprojection Imagery in Synthetic Aperture Radar," *IEEE Geoscience and Remote Sensing Letters*, vol. 9, no. 1, pp. 104–108, 2012.
22. F. Berizzi, E. Dalle Mese, and M. Martorella, "Performance analysis of a contrast-based ISAR autofocusing algorithm," in *Proceedings of the 2002 IEEE Radar Conference*, pp. 200–205, 2002.
23. Z. Lu, Z. Ding, and T. Long, "A novel Doppler ambiguity resolver based on contrast maximization," in *2012 IEEE Radar Conference*, pp. 0412–0415, 2012.
24. L. Zeng, Y. Liang, H. Wang, and M. Xing, "A weighted contrast enhancement autofocus algorithm," in *2015 IEEE 5th Asia-Pacific Conference on Synthetic Aperture Radar (APSAR)*, pp. 310–313, 2015.
25. H. Tang, H. Shi, and C. Qi, "Study on Improvement of Phase Gradient Autofocus Algorithm," in *2009 First International Workshop on Education Technology and Computer Science*, vol. 2, pp. 58–61, 2009.
26. R. L. J. Morrison and D. C. J. Munson, "An experimental study of a new entropy-based SAR autofocus technique," in *Proceedings. International Conference on Image Processing*, vol. 2, pp. II–II, 2002.
27. B. C. Flores, A. Ugarte, and V. Kreinovich, "Choice of an entropy-like function for range-Doppler processing," in *Automatic Object Recognition III* (F. A. Sadjadi,



- ed.), vol. 1960, pp. 47 – 56, International Society for Optics and Photonics, SPIE, 1993.
28. F. Berizzi and G. Corsini, “Autofocusing of inverse synthetic aperture radar images using contrast optimization,” *IEEE Transactions on Aerospace and Electronic Systems*, vol. 32, no. 3, pp. 1185–1191, 1996.
  29. L. Xi, L. Guosui, and J. Ni, “Autofocusing of ISAR images based on entropy minimization,” *IEEE Transactions on Aerospace and Electronic Systems*, vol. 35, no. 4, pp. 1240–1252, 1999.
  30. N. Pal and S. Pal, “Entropy: a new definition and its applications,” *IEEE Transactions on Systems, Man, and Cybernetics*, vol. 21, no. 5, pp. 1260–1270, 1991.
  31. S. L. Miller and D. Childers, *Probability and Random Processes: With Applications to Signal Processing and Communications*. Burlington, MA and San Diego, CA and London, UK: Elsevier Academic Press, 2004.
  32. S. M. Kay, *Fundamentals of Statistical Signal Processing: Detection Theory*. Upper Saddle River, NJ: Prentice-Hall, Inc., 1998.
  33. J. Stefanowicz, I. Ali, and S. Andersson, “Current trends in ship detection in single polarization synthetic aperture radar imagery,” in *Photonics Applications in Astronomy, Communications, Industry, and High Energy Physics Experiments 2020* (R. S. Romaniuk and M. Linczuk, eds.), vol. 11581, pp. 66 – 77, International Society for Optics and Photonics, SPIE, 2020.
  34. K. El-Darymli, P. McGuire, D. Power, and C. R. Moloney, “Target detection in synthetic aperture radar imagery: a state-of-the-art survey,” *Journal of Applied Remote Sensing*, vol. 7, no. 1, pp. 1–35, 2013.

## Acronyms

**CFAR** constant false alarm rate.

**CUT** cell under test.

**FFT** fast Fourier transform.

**i.i.d.** independent and identically distributed.

**IFFT** inverse fast Fourier transform.

**IQM** image quality metric.

**LFM** linear frequency modulated.

**MME** motion measurement error.

**NP** Neyman-Pearson.

**PD** probability of detection.

**PFA** polar (re)format algorithm.

**PSF** point spread function.

**RCS** radar cross section.

**RF** radio frequency.

**ROC** receiver operating characteristic.

**SAR** synthetic aperture radar.

**SCNR** signal-to-clutter-plus-noise ratio.

**SCR** signal-to-clutter ratio.

<b>REPORT DOCUMENTATION PAGE</b>					<i>Form Approved</i> <i>OMB No. 0704-0188</i>	
The public reporting burden for this collection of information is estimated to average 1 hour per response, including the time for reviewing instructions, searching existing data sources, gathering and maintaining the data needed, and completing and reviewing the collection of information. Send comments regarding this burden estimate or any other aspect of this collection of information, including suggestions for reducing this burden to Department of Defense, Washington Headquarters Services, Directorate for Information Operations and Reports (0704-0188), 1215 Jefferson Davis Highway, Suite 1204, Arlington, VA 22202-4302. Respondents should be aware that notwithstanding any other provision of law, no person shall be subject to any penalty for failing to comply with a collection of information if it does not display a currently valid OMB control number. <b>PLEASE DO NOT RETURN YOUR FORM TO THE ABOVE ADDRESS.</b>						
<b>1. REPORT DATE</b> (DD-MM-YYYY)		<b>2. REPORT TYPE</b>		<b>3. DATES COVERED</b> (From — To)		
16-06-2022		Master's Thesis		Aug 2019 — Jun 2022		
<b>4. TITLE AND SUBTITLE</b>				<b>5a. CONTRACT NUMBER</b>		
Effects of Motion Measurement Errors on Radar Target Detection				<b>5b. GRANT NUMBER</b>		
				<b>5c. PROGRAM ELEMENT NUMBER</b>		
<b>6. AUTHOR(S)</b>				<b>5d. PROJECT NUMBER</b>		
Capt Darnell D. Parker				<b>5e. TASK NUMBER</b>		
				<b>5f. WORK UNIT NUMBER</b>		
<b>7. PERFORMING ORGANIZATION NAME(S) AND ADDRESS(ES)</b>				<b>8. PERFORMING ORGANIZATION REPORT NUMBER</b>		
Air Force Institute of Technology Graduate School of Engineering and Management (AFIT/EN) 2950 Hobson Way WPAFB OH 45433-7765				AFIT-ENG-MS-22-J-015		
<b>9. SPONSORING / MONITORING AGENCY NAME(S) AND ADDRESS(ES)</b>				<b>10. SPONSOR/MONITOR'S ACRONYM(S)</b>		
Undisclosed				<b>11. SPONSOR/MONITOR'S REPORT NUMBER(S)</b>		
<b>12. DISTRIBUTION / AVAILABILITY STATEMENT</b>						
DISTRIBUTION STATEMENT A: APPROVED FOR PUBLIC RELEASE; DISTRIBUTION UNLIMITED.						
<b>13. SUPPLEMENTARY NOTES</b>						
<b>14. ABSTRACT</b>						
<p>This thesis investigates the relationships present between signal-to-clutter ratios, motion measurement errors, image quality metrics, and the task of target detection, in order to discover what factor merit greater focus in order to attain the highest probability of target detection success. This investigation is accomplished by running a high number of Monte Carlo trials through a coherent target detector and analyzing the results. The aforementioned relationships are demonstrated via sample synthetic aperture radar imagery, histograms, receiver operating characteristics curves, and error bar plots.</p>						
<b>15. SUBJECT TERMS</b>						
Motion measurement errors, image quality metrics, target detection, synthetic aperture radar						
<b>16. SECURITY CLASSIFICATION OF:</b>			<b>17. LIMITATION OF ABSTRACT</b>	<b>18. NUMBER OF PAGES</b>	<b>19a. NAME OF RESPONSIBLE PERSON</b>	
<b>a. REPORT</b>	<b>b. ABSTRACT</b>	<b>c. THIS PAGE</b>			Captain Darnell D. Parker, AFIT/ENG	
U	U	U	UU	90	<b>19b. TELEPHONE NUMBER</b> (include area code) (937) 255-3636	